JGR Atmospheres

Key Points:

- The vertical distribution of aerosol optical properties exhibits notable seasonal and regional differences using 15 years of Cloud-Aerosol Lidar with Orthogonal Polarization (CALIOP) data
- The trend of total aerosol optical depth (AOD) mainly depends on the joint changes of the highest frequency aerosol and the maximum AOD layer in a vertical profile
- The changes of AOD and main aerosol types in a region are also affected by the changes of aerosol transport sources and transport pathways

Supporting Information:

Supporting Information may be found in the online version of this article.

Correspondence to:

B. Chen,
chenbin@lzu.edu.cn

Author Contributions:

Conceptualization: Bin Chen, Jianping Huang
Data curation: Li Dong
Formal analysis: Bin Chen, Li Dong, Yixuan Wang, Zhikun Jing, Wei Yan, Xin Wang, Zhihao Song, Xuefeng Dong, Yue Huang
Methodology: Bin Chen, Li Dong
Writing – original draft: Bin Chen, Li Dong
Writing – review & editing: Bin Chen, Li Dong, Yixuan Wang, Zhongwei Huang, Xiaodan Guan

Analysis of Long-Term Trends in the Vertical Distribution and Transport Paths of Atmospheric Aerosols in Typical Regions of China Using 15 Years of CALIOP Data

Bin Chen[1,2] , **Li Dong**[1,3], **Jianping Huang**[1,2] , **Yixuan Wang**[1,2], **Zhikun Jing**[1,2], **Wei Yan**[1,2], **Xin Wang**[1,2] , **Zhihao Song**[1,2], **Zhongwei Huang**[1,2] , **Xiaodan Guan**[1,2] , **Xuefeng Dong**[4], and **Yue Huang**[5]

[1]College of Atmospheric Sciences, Lanzhou University, Lanzhou, China, [2]Collaborative Innovation Center for Western Ecological Safety, Lanzhou University, Lanzhou, China, [3]Tianshui Meteorological Bureau, Tianshui, China, [4]Sanshui District Meteorological Bureau, Foshan, China, [5]Eco-Environmental Science Research and Design Institute of Zhejiang, Hangzhou, China

Abstract Long-range transport and vertical distribution of aerosols are important factors for assessing the uncertainty in aerosol radiative forcing. This paper reveals the vertical distribution and trends of aerosol optical properties in China using 15 years of Cloud-Aerosol Lidar with Orthogonal Polarization (CALIOP) data. The Hybrid Single-Particle Lagrangian integrated trajectory model was used to analyze the transport and trends of aerosols in the layer with the highest occurrence frequencies of dust, polluted dust, polluted continental and elevated smoke aerosols. The results indicated that (a) there were significant regional and seasonal differences in the vertical distribution of aerosols. The aerosol optical depth (AOD) trend in a given region depends on the changes in the aerosol type with the highest frequency and the layer corresponding to the largest AOD in the vertical profile. The frequency of polluted dust aerosols was the highest in Beijing-Tianjin-Hebei (BTH) and Central China. The considerable decrease in the 0–2 km AOD led to a significant trend of the column AOD. (b) The changes of AOD and main aerosol types in a region are also affected by the changes of aerosol sources and long-range transport pathways. In the BTH, dust aerosols originated from the Mongolian Plateau, accounting for 57.88% of the total trajectories. The Pearl River Delta was dominated by elevated smoke aerosols, with trajectories mainly originating from the Myanmar and Vietnam, accounting for 27.38% and 29.59%, respectively. The trend of 15-year backward trajectories of dust aerosols on the Tibetan Plateau indicated that the trajectory from India is increasing.

Plain Language Summary Aerosols are one of the main factors affecting global climate change, influencing global radiation through direct and indirect effects. Long-range transport aerosols and their vertical distribution are important factors for assessing the uncertainty in aerosol radiative forcing. At present, there is limited research on the vertical distribution and transport pathways of different types of aerosols in multiple regions over China. Considering that aerosols in different regions of China exhibit large vertical distribution and transport differences, we revealed the vertical distribution and trends of aerosol optical properties in China using 15 years of Cloud-Aerosol Lidar with Orthogonal Polarization data. The Hybrid Single-Particle Lagrangian Integrated Trajectory model was used to analyze the transport and trends of different aerosols. We found significant regional and seasonal differences in the vertical distributions of aerosols. The changes in the aerosol optical depth and main aerosol types in a given region were also significantly affected by the changes in aerosol transport sources and transport pathways. This study provides comprehensive insight into the vertical distribution and transport characteristics of different types of atmospheric aerosols in the Chinese region over the last 15 years, which is very important to further evaluation of the impact of different aerosol types on the radiative effects and the environment.

1. Introduction

The sixth report of the Intergovernmental Panel on Climate Change identified atmospheric aerosols as one of the main factors affecting global climate change (Veal, 2021). Aerosols directly affect the climate by absorbing and scattering solar shortwave radiation and altering the energy balance in the ground-air system and indirectly affect it by functioning as cloud condensation nuclei or ice nuclei and influencing precipitation processes (Andreae

et al., 1988; Wang et al., 2010). Aerosol-induced changes in monsoon circulation may further influence vertical wind shear due to circulation, leading to enhanced tropical cyclones (Ganguly et al., 2012; Wang & Hao, 2012).

The lack of knowledge on the long-term vertical distribution of aerosols is one of the main reasons for the uncertainty in assessing the radiative climate effects of aerosols (Chung et al., 2005; Mishra & Shibata, 2012). The vertical distribution of aerosols not only significantly impacts their lifetime and spatial distribution (Charlson et al., 1992; Wang et al., 2018) but also significantly impacts the radiative heating rate, thermal structure and stability of the atmosphere (Chen et al., 2007; Huang et al., 2015). The variation in the thermal structure of the atmosphere due to the vertical distribution of aerosols affects the ability to disperse atmospheric pollution, causing air pollution events (Wang et al., 2018). The vertical distribution of aerosols determines the formation of cloud anvils and cloud condensation nuclei and the extent to which the cloud microphysical processes and precipitation are impacted (Fridlind et al., 2004). It has been shown that aerosols in the mid-troposphere (3–10 km) impose a great influence on cloud properties (Lebo, 2014), and aerosols in the lower troposphere exert a great influence on mixed-phase precipitation (Marinescu et al., 2017). In addition, the vertical distribution of aerosols determines the mechanisms by which aerosols enter clouds from different heights (Zhang et al., 2021), thus affecting precipitation. However, different types of aerosols have varied effects on precipitation (Ramanathan et al., 2001; Rosenfeld et al., 2008). In contrast to the inhibition of convection by smoke aerosols, dust and polluted continental aerosols are more likely to promote convection, thereby enhancing precipitation (Jiang et al., 2018; Wang et al., 2015). In addition, urban air pollution and smoke stemming from fires can absorb sunlight to reduce cloud formation, thus cooling the surface and heating the atmosphere (Koren et al., 2004).

The Cloud-Aerosol Lidar with Orthogonal Polarization (CALIOP) onboard the Cloud-Aerosol Lidar and Infrared Pathfinder Satellite Observation (CALIPSO) satellite launched in 2006, is a polarimetric lidar with dual wavelengths of 1,064 and 532 nm wavelengths, which are used to detect the vertical structure and interactions of clouds and aerosols worldwide. The CALIOP instrument is the world's first applied satellite-based cloud and aerosol lidar (Winker et al., 2004a, 2006). It provides high-resolution global aerosol vertical profile information and facilitates the study of the vertical distribution (Winker et al., 2007).

Mehta et al. (2018) found a global trend of decreasing particulate matter column loads based on CALIOP data, with an increase in the total aerosols in India and significant decreases in the total aerosol loads in North America, South America, eastern China and Australia (Brakhasi et al., 2021; Ratnam et al., 2021). Moreover, the vertical distribution of global aerosols significantly differs among various regions (Amiridis et al., 2010; Kim et al., 2021; Liu et al., 2021; Ma & Yu, 2014; VanCuren, 2003). Due to the complex urban clusters and unique geographical conditions in China, there are significant regional differences in the vertical distribution of aerosols. The aerosols in Zhejiang are concentrated at heights of 1–2 km above the ground in spring and summer, but they mainly occurring below 1 km in winter and at high altitudes in autumn (Yu et al., 2021). In April, the aerosols in the Nanjing region are dominated by dust and polluted dust aerosols (Shen & Cao, 2020). Huang et al. (2007) also found that the Tibetan Plateau (TP) is dominated by dust and polluted dust aerosols, which generally occur at altitudes from 4 to 7 km and rise to a maximum altitude of 10 km or higher (Liu et al., 2008). In addition, Li et al. (2015), using CALIOP data, found that the aerosols in Shanxi Province were mainly distributed in the 0–2 km range, with fine particles dominating at lower levels, whereas above 2 km, aerosols were influenced by transmitted dust aerosols, exhibiting larger aerosol particle sizes.

The sources, particle size distribution and characteristics of different types of aerosol particles vary considerably among different seasons and regions (Yang et al., 2021), and local aerosol types and corresponding distributions can vary due to the effects of long-range aerosol transport (Babu & Sivaprasad, 2014; Kim et al., 2021; Lakshmi et al., 2021; VanCuren, 2003). The aerosols in Shanghai might be affected by the long-range transport of dust in spring, and the shape of aerosol particles in the middle and upper troposphere is more irregular than that of aerosol particles in the lower troposphere (Chen et al., 2012). Below 4 km, Beijing is dominated by polluted dust aerosols. Due to the large-scale transmission of aerosols from Mongolia and the Gobi Desert west of mainland China, the occurrence frequency of dust aerosols in Beijing is also high (Zhang et al., 2009). Previous studies have demonstrated that long-distance transport of aerosols can lead to significant variations in the aerosol optical properties and distribution (Chen et al., 2022; Han et al., 2022; McKendry et al., 2011; Ramanathan & Feng, 2009).

Although the vertical distribution and transport pathways of atmospheric aerosols in China have been studied, these factors have mainly been characterized through the analysis of individual regions over a short period, but few studies have examined different types of aerosols. Therefore, this paper analyzed the vertical distribution

and trends of different types of aerosols in 10 typical regions of China using CALIOP data from June 2006 to December 2020. Combined with the Hybrid Single-Particle Lagrangian Integrated Trajectory (HYSPLIT) model, which was adopted to analyze the transport paths of aerosols in the different regions, the trends of forward and backward transport processes of the four main aerosols were analyzed (Stein et al., 2015). This research work provide a scientific basis for future research on the climatic effects of aerosols and management of the atmospheric environment.

2. Data and Methods

2.1. CALIOP

The main payload of the CALIPSO satellite includes the CALIOP (Liu et al., 2012; Winker, Hostetler, & Hunt, 2004), Imaging Infrared Radiometer and Wide Field Camera (Ou et al., 2017). The CALIOP Level 1 data include the 532/1,064 nm extinction backscatter signal, payload status and more. The Cloud and Aerosol Profile product (Level 2 Profile) includes vertical profile information on optical properties such as aerosol extinction coefficients (AECs) and backscatter coefficients; the Vertical Feature Mask (Level 2 VFM) Product includes cloud and aerosol types and cloud phase (Winker et al., 2007). Level 3 tropospheric aerosol profiling products are obtained from Level 2 products with a strict quality filter, providing monthly gridded cloud and aerosol data with a spatial resolution of $2° \times 5°$. The CALIOP data have been updated to version 4 (V4), and relative to version 3 products, the V4 data product provides improved cloud-aerosol discrimination (CAD) algorithms and extinction QC flags, as well as the inclusion of a new aerosol type (dust marine) (Kim et al., 2018).

The VFM product from June 2006 to December 2020 was used in this study, and it including seven tropospheric aerosol types (clean marine, dust, polluted continental, clean continental, polluted dust, elevated smoke and dust marine). The CALIOP CAD V4 algorithm uses altitude, location, surface type, particulate depolarization ratio (PDR), and integrated attenuated backscatter to identify the aerosol subtype. The Level 2 profile products with a vertical resolution of 60 m can provide the optical properties of aerosols, such as the AEC, PDR and Color ratio (CR). CR was obtained by dividing the backscatter coefficient at 1,064 nm by that at 532 nm to characterize the particle size). Aerosol extinction coefficients refers to the extinction cross section of aerosol particles, which represents the extinction characteristics of aerosols. The integration of AEC along the vertical direction yields the AOD. Particulate depolarization ratio is defined as the ratio of the perpendicular to parallel components of the aerosol backscatter coefficients at 532 nm wavelength (Mehta et al., 2021). Yang et al. (2012) suggested that the PDR depends on the shape of the particles, with PDR values greater than 0.2 indicating dust and 0.075 < PDR <0.2 indicating polluted dust (Omar et al., 2009), which suggests that more spherical particles are present in polluted dust while more nonspherical particles are present in dust (Muller et al., 2003; Shimizu et al., 2004).

CAD scores are used to express the confidence in aerosol or cloud classification. The CAD scores reported in the CALIPSO layer products vary between −100 and 100. A positive CAD score indicates clouds and a negative value represents aerosols. The absolute value of the CAD score provides a confidence level for classification (Winker et al., 2013). According to Young et al. (2018), QC flag values of 0, 1, 16, or 18 can be applied for reliable scientific analysis. In this study, the CAD and QC flags were used to control the quality of the data. The selection range of CAD is −100 to −70, and the extinction QC flags is 0, 1, 16, and 18. In addition, the column AOD of all aerosols, dust aerosols, polluted dust aerosols and elevated smoke aerosols provided by Level 3 data products was also used. Because of the low signal-to-noise ratio of CALIOP data during the daytime (Liu et al., 2009; Zheng et al., 2022), therefore, the data used in this study were all nighttime observations.

2.2. HYSPLIT Model

HYSPLIT (https://www.arl.noaa.gov/HYSPLIT.php) model is a trajectory model developed by the National Oceanic and Atmospheric Administration to analyze the transport and dispersion of air pollution using a hybrid Lagrangian-Eulerian calculation (Draxler, 2003; Draxler and Hess, 1997, 1998). One of the most common applications of the model is back trajectory calculation to determine the source of air masses and establish source-receptor relationships (Fleming et al., 2012). Trajectories are usually used to track or predict the movement of air masses (Stein et al., 2015). HYSPLIT has also been used in various simulation studies to describe the transport, dispersion and deposition of pollutants and hazardous substances in the atmosphere (Abdalmogith & Harrison, 2005; Cohen et al., 2004; Draxler et al., 2015; Srinivas et al., 2012). To investigate the characteristics of

aerosol transport, the HYSPLIT model was used to simulate the 48 hr backward and forward aerosol trajectories in 10 typical regions in China. The HYSPLIT external meteorological element field is a global data assimilation and prediction system (GDAS) data set (spatial resolution 1°) from 2006 to 2020 (Su et al., 2015).

To better understand the transport characteristics of the different types of aerosols over the years, we analyzed the frequency of trajectories by calculating the number of trajectories within each grid cell covering the region. The grid resolution defaults to 1.0°. We determined whether each trajectory intersects with each grid cell. If it intersects once, the trajectory is recorded as crossing this grid cell once. The track frequency ($F_{i,j}$) of each grid cell (i, j) can be obtained by dividing the number of trajectories (T) of all trajectories passing through the grid cell by the total number of trajectories (N), as expressed in Formula 1:

$$F_{i,j} = 100 \sum T_{i,j}/N \tag{1}$$

The trajectories of the different types of aerosol transport were clustered and their trend changes were studied. The approach used to cluster trajectories involved determining the transport direction and distance of each track in the HYSPLIT model, and the final number of clusters was determined based on the total spatial variance (TSV). In the process of clustering, the SV between each endpoint (k) was calculated along the trajectory (n) of the mth cluster (m):

$$SV_{m,n} = \sum_k (P_{n,k} - M_{m,k})^2 \tag{2}$$

where P and M are the position vectors of a single trajectory and the average trajectory of the mth cluster, respectively. The clustered spatial variance (CSV) is the sum of the spatial variances of all trajectories of the mth cluster:

$$CSV_m = \sum_n SV_{m,n} \tag{3}$$

Moreover, the TSV is the sum of the CSV values of all clusters:

$$TSV = \sum_m CSV_{m,k} \tag{4}$$

In this process, the TSV first rises rapidly, and then remains stable in the remaining iterations until the end of the calculation. At this time, the different clusters begin to merge and the TSV rises again. The ideal final number of clusters is that before the second increase in the TSV (Borge et al., 2007; Dorling et al., 1992).

3. Results and Discussion

3.1. Spatial and Temporal Distributions of Aerosols in China

Figure 1 shows the spatial distribution of the average AOD in China from June 2006 to December 2020. China's regions with high column AOD values are predominantly located in central and southern parts of the country (Figure 1a), which is related to the frequent human activities and notable industrial production activities in these regions (Chen et al., 2021; Zhang et al., 2020). Low-value regions were mostly observed in the TP region. High dust AOD values (Figure 1b) were concentrated in the Taklamakan Desert (TD), which is the most important source area of dust aerosols in East Asia. High polluted dust AOD values (Figure 1c) were mainly distributed in northern China and Central China (CC) due to the notable anthropogenic activities and accelerated urbanization over the last years (He et al., 2017; Sun et al., 2022). Regions with high elevated smoke AOD values (Figure 1d) were largely located in South China and CC, especially in the Pearl River Delta (PRD) region, which is influenced by the transport of elevated smoke aerosols emitted during the combustion of organic matter in Southeast Asia (Cao et al., 2008; Che et al., 2015).

The AOD spatial distribution of various aerosol types in different regions obviously varied, and 10 study regions were defined according to the distribution, as shown in the box in Figure 1a, namely, Beijing-Tianjin-Hebei (BTH), CC, Cheng-Yu (CY) District (CY), Yangtze River Delta (YRD), PRD, Guanzhong Plain region (GZ), Alashan and Ordos Plateau region (AOP), TD, TP and North East China (EN), and the average surface elevation of each region in Table S1 in Supporting Information S1.
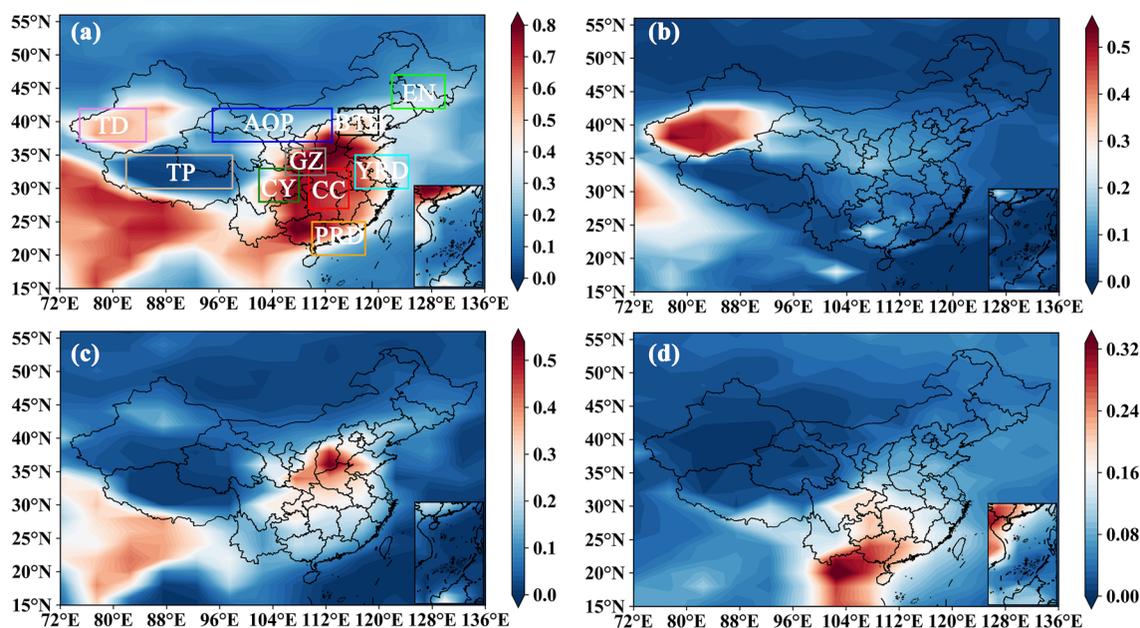
Figure 1. Spatial distribution of column aerosol optical depth (AOD) (a), dust AOD (b), polluted dust AOD (c) and elevated smoke AOD (d) in China from June 2006 to December 2020, and the boxes in (a) show the 10 typical regions studied.

3.2. Long-Term Changes in the Vertical Distribution of Aerosol Optical Properties

3.2.1. Time Series Variation in the Aerosol Optical Properties

Figure 2 shows the annual mean AEC vertical distribution of aerosols in each region from June 2006 to December 2020. The AEC values were higher in CC, Guanzhong Plain region (GZ), and CY District (CY), peaking at 0.5 km^{-1}, with lower values in the TP and North East China (EN) regions. In terms of the vertical distribution, the AEC decreased with increasing altitude in all regions. High AEC values (>0.05 km^{-1}) on the TP were distributed at altitudes ranging from 4 to 6 km (above the mean sea level in the article), high AEC values (>0.2 km^{-1}) in the
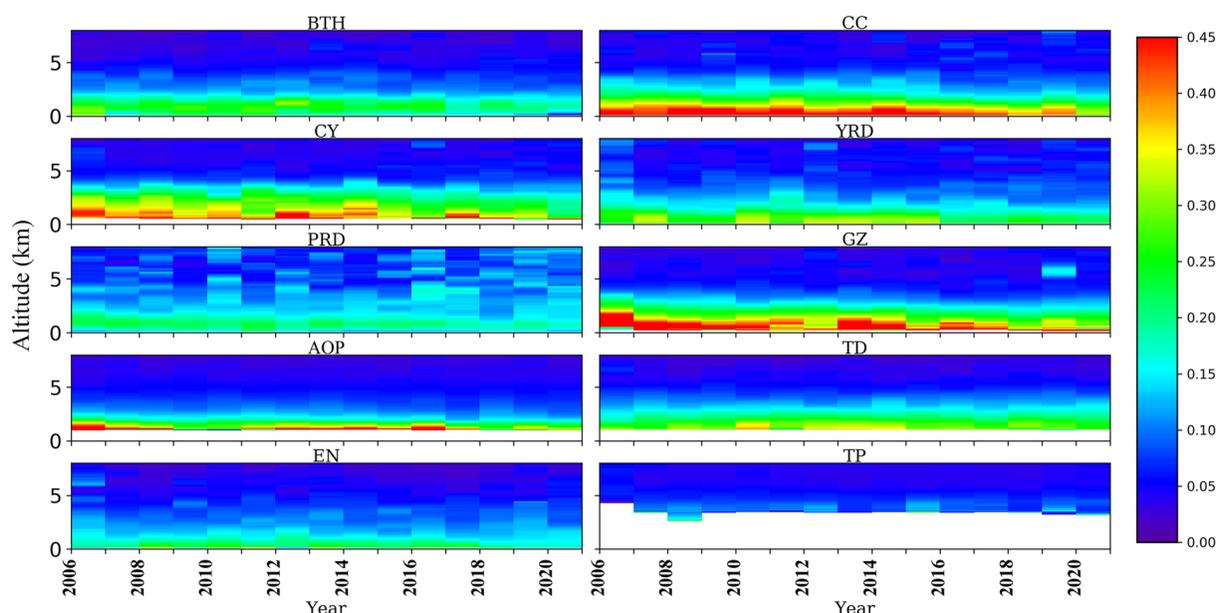

Figure 2. Vertical distribution of aerosol annual average aerosol extinction coefficient from June 2006 to December 2020 (Unit: km^{-1}, altitude means above mean sea level).
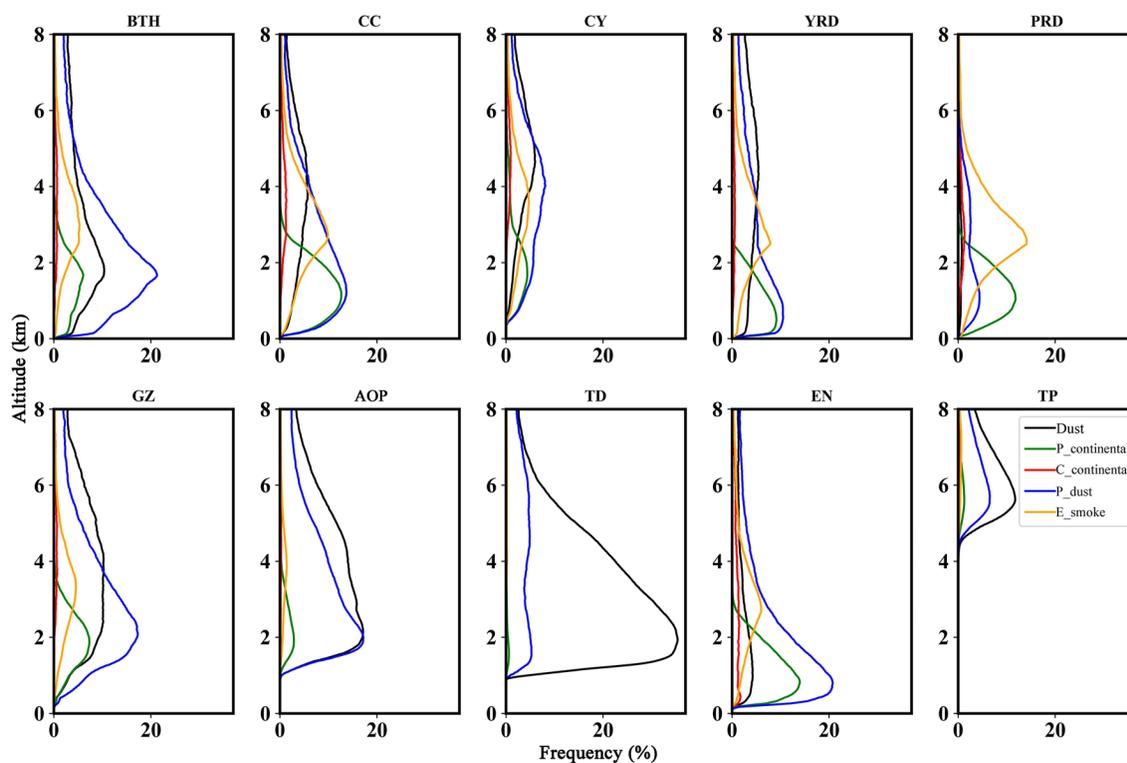
Figure 3. Vertical profile of the multi-year average occurrence frequency of different aerosol types in the study region from June 2006 to December 2020, with altitude indicating higher than mean sea level.

TD, CY and Alashan and Ordos Plateau region (AOP) occurred at altitudes from approximately 2-3 km, high AEC values (>0.2 km^{-1}) in the remaining regions were mainly distributed at altitudes from 0 to 3 km. High AEC values were observed in all regions at altitudes from 0 to 3 km. High AEC values for dust aerosols were mainly observed in dust source areas (Figure S1 in Supporting Information S1), such as the TD, and the AEC gradually decreased over time. The polluted continental and polluted dust AEC values were high in Beijing-Tianjin-Hebei (BTH), CC, CY, YRD, GZ and EN, reflecting high anthropogenic emissions, with AEC values higher than 0.05 km^{-1} ranged from 0 to 4 km. Elevated smoke AEC values were high in the PRD region, with high values ranging from 0 to 0.18 km^{-1} above 4 km, which could be influenced by transport (Ding et al., 2021). The PDR value in regions of TD and AOP were relatively high, ranging from 0 to 0.35, and high PDR values (>0.2) were distributed within 2–6 km range (Figure S2 in Supporting Information S1). The vertical distribution of the CR in these two regions was very similar to that of the PDR (Figure S3 in Supporting Information S1), with the CR values ranging from 0.75 to 1.0 at altitudes from 2 to 6 km. These two regions were mainly dominated by dust and polluted dust aerosols, which also indicated that irregular and coarse particles are the main particles. High PDR values (>0.1) were mainly distributed above 5 km in BTH, GZ, CC, CY, YRD, and EN, and the CR was >0.8 above 5 km. Due to long-range transport of dust aerosols, above 4 km, higher PDR (>0.15) and CR (>0.7) values were observed for aerosol particles in these regions. The AEC below 4 km in CC, CY, GZ, and EN has decreased annually since 2015, which could be attributed to the effective measures implemented by the Chinese government to reduce anthropogenic emissions in recent years (Dong et al., 2021; Gui et al., 2021; Zheng et al., 2018).

3.2.2. Frequency of Aerosols

Due to the influences of local anthropogenic emissions and aerosol transport, the main aerosol types significantly varied in the different regions. Figure 3 shows the vertical distribution of the occurrence frequency in the different types of aerosols, the aerosol types and altitude with the highest frequency in all regions are listed in Table S2 in Supporting Information S1. The frequency of a given aerosol type is the number of samples on the days of its occurrence divided by the total number of samples (all aerosol types and clean air types). The results indicated that dust aerosols most frequently occurred in the TD region, mainly at altitudes from 1.5 to 5.5 km, and the maximum frequency, namely 36%, was reached at approximately 2 km. Moreover, the AOP is influenced by the
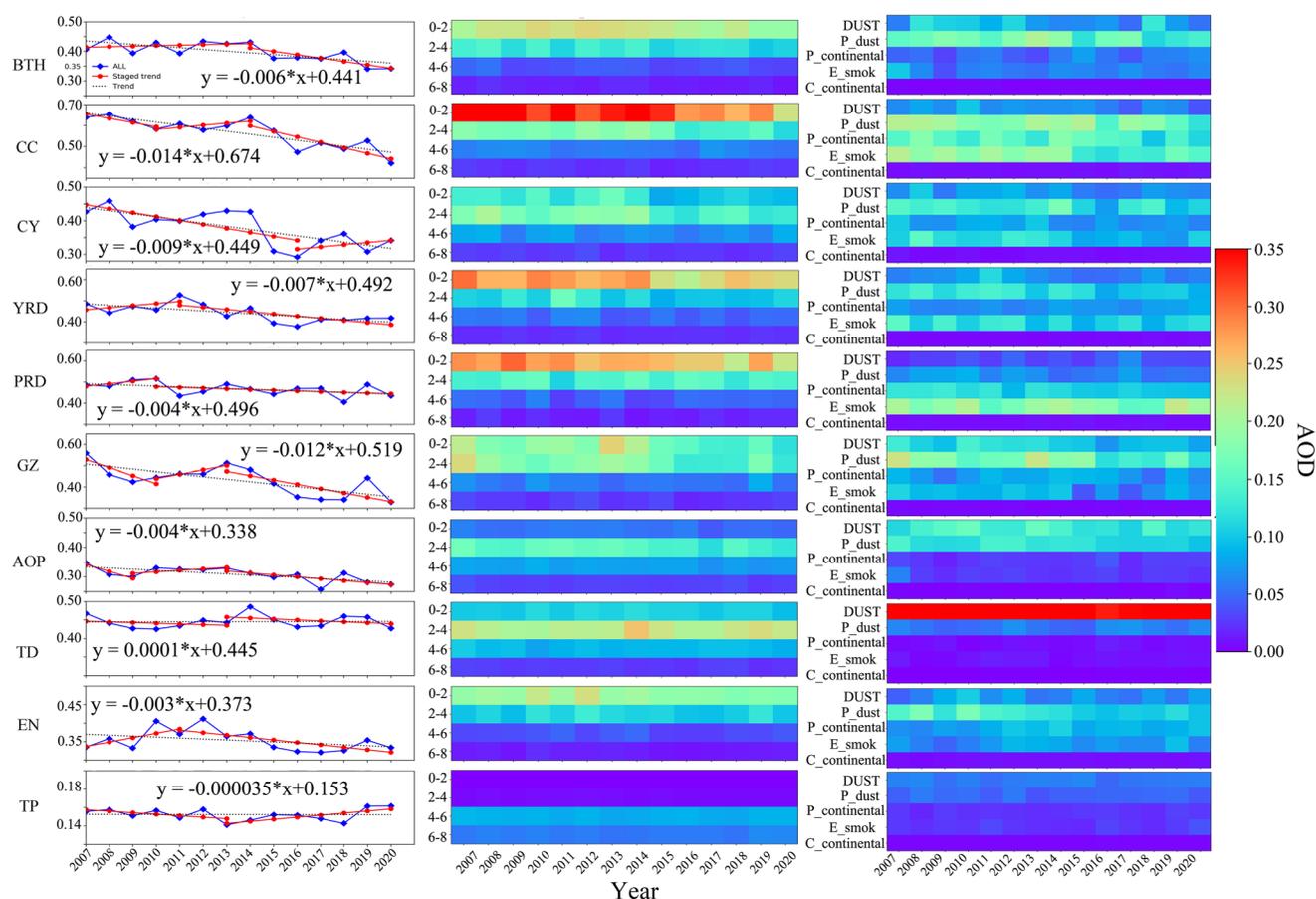
Figure 4. The trend of aerosol optical depth (AOD) in the study region. Left column: blue, red, and black dashed lines are annual mean AOD, trend of annual mean AOD at different phases of division and trend of annual mean AOD from 2007 to 2022; Middle column: Annual mean AOD at altitudes from 0 to 2, 2–4, 4–6, 6–8 km; Right column: Annual mean AOD of dust, polluted dust, polluted continental, elevated smoke and clean continental.

Mu Us Desert, Badain Jaran Desert and Ulan Buh Desert, where the dust aerosol frequency reached 17% at 2 km. Dust was also the predominant aerosol type across the TP, with a maximum frequency of 12% at 5.5 km above mean sea level, which is associated with dust aerosol transport from the field to the TP (Huang et al., 2007; Yuan et al., 2019). The maximum frequencies of dust aerosols in BTH and GZ, reaching approximately 10%, were observed at 2 and 4 km, respectively. Many studies have shown that dust aerosols originating from Northwest China and Mongolia can be transported to BTH and GZ (Huang et al., 2008), and the long-range transport dust is one of the important contributors to PM10 during haze periods in these regions (Chen, Song, Huang, et al., 2022).

The BTH, CC, CY, YRD, PRD, and GZ regions in China exhibit high levels of anthropogenic emissions. Therefore, polluted dust and polluted continental aerosols were also the main aerosol types in these regions. Especially in the BTH, the frequency of polluted dust aerosols reached 21% at 1.7 km. The highest frequency of polluted dust aerosols occurred in the CC, CY, YRD, and GZ at altitudes of 1.5, 4, 1, and 2 km, respectively. The highest frequency of polluted continental aerosols in these regions was observed at 0–2 km. In addition, the frequency of polluted continental aerosols in the BTH, CY, AOP, TD, and TP was less than 4%. Elevated smoke aerosols are mainly generated via biomass combustion and they constituted one of the main aerosol types in the CC and PRD, mostly occurring at altitudes from 2.5 to 5.5 km, with maximum frequencies of 9% and 14%, respectively. However, the frequency of clean continental aerosols was low, with a maximum frequency of 2% observed in EN.

3.2.3. Changes in the Aerosol AOD Trends

The annual mean values of the total AOD (Figure 4, left column), AOD at the different altitudes (middle column) and AOD of the different types of aerosols (right column) from 2007 to 2020 were calculated. The least squares method was used to fit the change trend of the annual mean AOD value, and the change characteristics of the

total AOD in the different regions were analyzed. We also divided the trend into different phases according to the trend direction (left column, red line). It was observed that decreasing trend of column AOD values existed in all regions except for the TD and TP. The column AOD values in the BTH, YRD, PRD, and EN first increased and then decreased. The decreasing AOD trend in BTH was influenced by 0–2 km aerosols, especially polluted dust aerosols, because the AOD from 0 to 2 km accounted for more than 50% of the total AOD in BTH (Figure S4 in Supporting Information S1) and the region was dominated by polluted dust aerosols (Figure 3). After 2014, the AOD at altitudes from 0 to 4 km significantly decreased in BTH, and the dust, polluted dust and elevated smoke AOD values also decreased. The column AOD in the YRD region increasing until 2011 and then started to decrease after 2011, mainly due to the influence of 0–2 km aerosols which accounted for 58% of the total AOD and consisted mainly of polluted dust aerosols. The PRD region exhibited a decreasing trend of the AOD after 2010, mainly because the AOD values of polluted continental, polluted dust, and elevated smoke aerosols decreased, especially at altitudes from 0 to 4 km, which accounted for more than 80% of the total AOD. The AOD at altitudes from 0 to 4 km in EN increased before 2012 and significantly decreased after 2012, accounting for 84% of the overall decrease. The changes in the frequency of polluted continental, polluted dust and elevated smoke aerosols were similar to those in the column AOD in EN.

The AOD trends in CC, GZ, and AOP first increased and then decreased. The AOD in CC first decreased and then increased before 2014 and again decreased thereafter, mainly driven by the AOD from 0 to 4 km (accounting for over 84% of the total AOD). This was especially evident in the polluted continental and polluted dust aerosols, further validating the dominance of these two aerosols in CC. The AOD in GZ decreased before 2010 and then increased, but after 2013, the AOD significantly decreased. This trend was driven mainly by the changes in the AOD from 0 to 4 km (accounting for 79% of the total AOD), and the AOD values of dust, polluted continental and polluted dust aerosols exhibited the same trend as that of the column AOD. The AOD in the AOP exhibited a slightly increasing trend from 2009 to 2013, with the main AOD change occurring from 2 to 4 km, accounting for 47% of the total AOD variation. The AOD of dust aerosols in this region exhibited the same change. After 2013, a decrease in the dust and polluted dust aerosols in the AOP led to a decrease in the column AOD.

The AOD in CY decreased initially, then increased with a slight increase after 2016 due to changes occurring in the AOD levels between 2 and 4 km, which accounted for over 40% of the total AOD variation (Figure S4 in Supporting Information S1). A slight increase in dust, polluted dust and elevated smoke AOD values was also observed. On the TP, the AOD exhibited an initial decreasing trend followed by an increasing trend in 2013, but the overall column AOD change was not obvious. In terms of the different altitudes and various types of aerosols, the AOD variation could be mainly attributed to aerosols at altitudes from 4 to 6 km, accounting for up to 55% of the column AOD. The column AOD in the TD region exhibited nonsignificant change, that was similar to that on the TP. However, there occurred a decreasing AOD trend in the TD region after 2014, mainly because of the AOD at altitudes from 2 to 4 km, which accounting for approximately 49% of the total AOD, and especially because of the influence of dust aerosols. In contrast, the polluted dust AOD value tended to slightly increase.

3.3. Seasonal Average Optical Properties of Aerosols

Figure 5 shows the seasonal variation characteristics of the AEC vertical distribution of the different types of aerosols. Except for those on the TP (due to the influence of the elevation of the Qinghai Tibet Plateau), the high AEC values in the other regions were mainly distributed from 0 to 4 km during each season. The AEC in Beijing-Tianjin-Hebei (BTH) was the highest in summer (Sun et al., 2017), especially from 1 to 2 km, and the AEC reached 0.25 km^{-1}. The AEC of polluted dust and polluted continental aerosol was the highest in summer, whereas the AEC of dust aerosols was the highest in spring. Based on the PDR (Figure S5 in Supporting Information S1) and CR (Figure S6 in Supporting Information S1), the particles were more regular and finer in summer than in spring. The AEC values in CC, CY District, and Guanzhong Plain region (GZ) were the highest in winter, followed by autumn. These regions were dominated by polluted dust aerosols, and the AEC of polluted dust aerosols was the highest in winter. The AEC in the PRD region was also higher in autumn and winter than that in the other seasons because the AEC of polluted continental aerosols was high in autumn and winter, namely, greater than 0.1 km^{-1} at approximately 1.5 km. The AEC of elevated smoke aerosols was high above 4 km in autumn and winter but reached 0.13 km^{-1} in spring at approximately 3 km. In contrast, the PDR in the PRD region was the lowest among the studied regions. The total mean AEC values in the YRD and Alashan and Ordos Plateau region (AOP) were higher in winter than in the other seasons, and the maximum AEC value from 0 to 1 km exceeded 0.25 km^{-1} in the
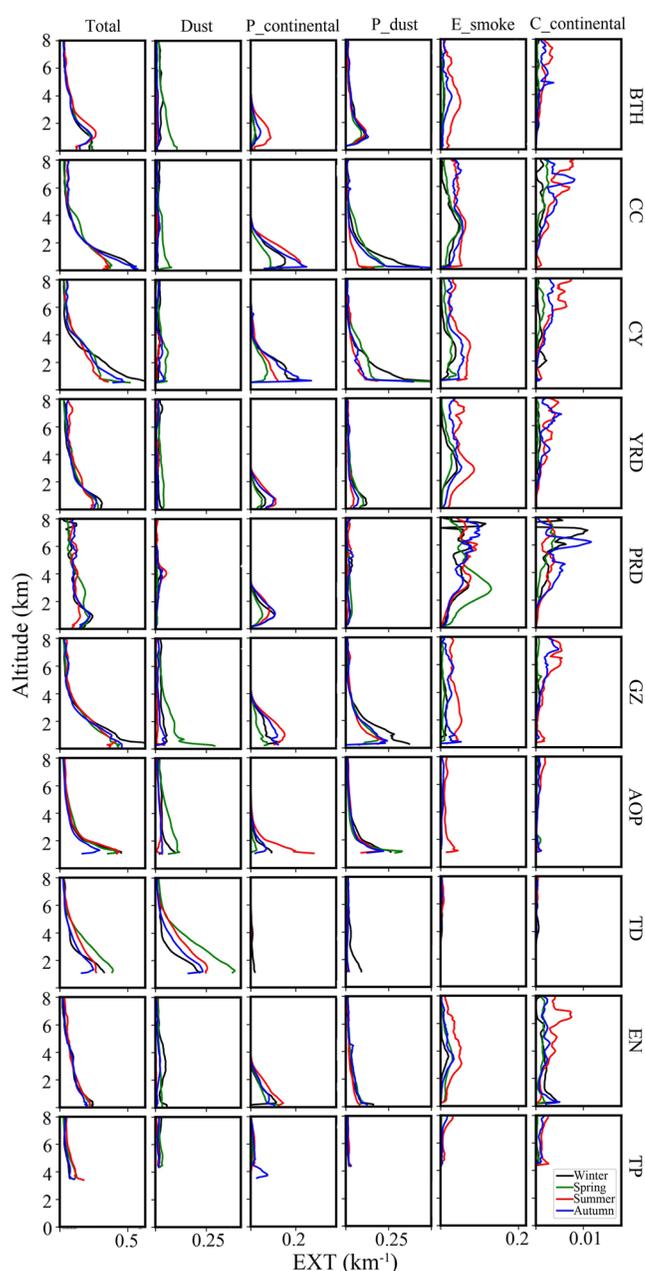
Figure 5. The vertical distribution of seasonal (spring: green line; summer: red line; autumn: blue line; winter: black line) average aerosol extinction coefficient (EXT) for the 10 regions during the study period (row) from June 2006 to December 2020, including the Total mean (Column 1), dust (Column 2), polluted continental (Column 3), polluted dust (Column 4), elevated smoke (Column 5) and clean continental (Column 6) extinction coefficient (Unit: km^{-1}).

YRD. In the YRD, the AEC values of dust and polluted dust aerosols were the highest in winter and spring, whereas the AEC values of polluted continental aerosols and elevated smoke aerosols were the highest in summer. The maximum total mean AEC in the AOP at an altitude of the 1.5 km was higher than 0.4 km^{-1}. The AEC values of dust and polluted dust aerosols were the highest in winter and spring, and the AEC values of polluted continental aerosols was the highest in summer, reaching up to 0.28 km^{-1}. The AEC in the TD was the highest in spring and reached a maximum value of 0.4 km^{-1} at 1.5 km, mainly due to the contributions of dust aerosols. The maximum AEC value reached 0.38 km^{-1} in spring. The PDR and CR in the TD region were high at altitudes from 2 to 4 km, indicating that the aerosol particles in this region were mostly irregular and relatively larger in size. In addition, the PDR value above 2.5 km decreased with altitude, indicating that the shape of the particles became less nonspherical. The seasonal AEC differences on the TP were limited, with the predominantly dust and polluted dust aerosols in this region exhibiting the highest AEC values. Furthermore, coarser particles were observed in winter and spring, which could be related to the transport of dust aerosols from northern India and the TD to the TP in spring.

The optical properties of each aerosol type in the different regions have obvious seasonal variations. To determine the dominant aerosol types in the study regions during the different seasons, the seasonal average proportion of aerosols is shown in Figure 6 (the proportion is calculated by dividing the sample size of a certain type of aerosol by the sample size of all aerosol types at the corresponding altitude). In BTH, dust aerosols accounted for the highest proportion in winter and spring (>40%), and polluted dust aerosols accounted for the highest proportion in summer and autumn, especially in autumn (43.7%). In CC, CY and North East China (EN), polluted dust aerosols accounted for the highest proportion in winter and spring (>37%), but in summer and autumn, the proportion of elevated smoke and polluted continental aerosols was higher, especially in CC, with values of 48.9% and 21.91%, respectively. In the YRD region and GZ, dust aerosols accounted for the highest proportion in winter and spring, with GZ exhibiting a high proportion of 48% in spring. Elevated smoke aerosols accounted for the highest proportion (≥38%) in the YRD region, while polluted dust aerosols in GZ accounted for the highest proportion (≥35%) in summer and autumn. In the TD region, the proportion of dust aerosols during all seasons was the highest, at 56% (winter), 86% (spring), 72% (summer) and 68% (autumn). The proportions of polluted dust aerosols in autumn and winter were 27% and 34%, respectively. On the TP, except for the higher proportion of polluted dust aerosols (28%) in summer, dust aerosols accounted for the highest proportions of 57%, 56% and 33%, during the other seasons. Notably, polluted continental aerosols exhibited 29% proportion in autumn.

3.4. Typical Paths of Aerosol Transport

Figure 3 shows that dust aerosols, followed by polluted dust aerosols, most frequently occurred in dust source areas. Moreover, polluted continental and elevated smoke aerosols also occurred in dust source areas due to aerosol transport. Additionally, due to transport from other regions, the occurrence frequency in anthropogenic source areas was the highest for dust aerosols, followed by polluted continental aerosols and elevated smoke aerosols. Therefore, the HYSPLIT model was used to simulate the transport pathways of the different aerosols in the study regions. The centers of the study regions were selected as the trajectory end or starting point of the trajectory (Table S1 in Supporting Information S1). The 48 hr backward and forward aerosol trajectories were simulated using the HYSPLIT model. As the vertical altitude of the annual average occurrence frequency of each aerosol
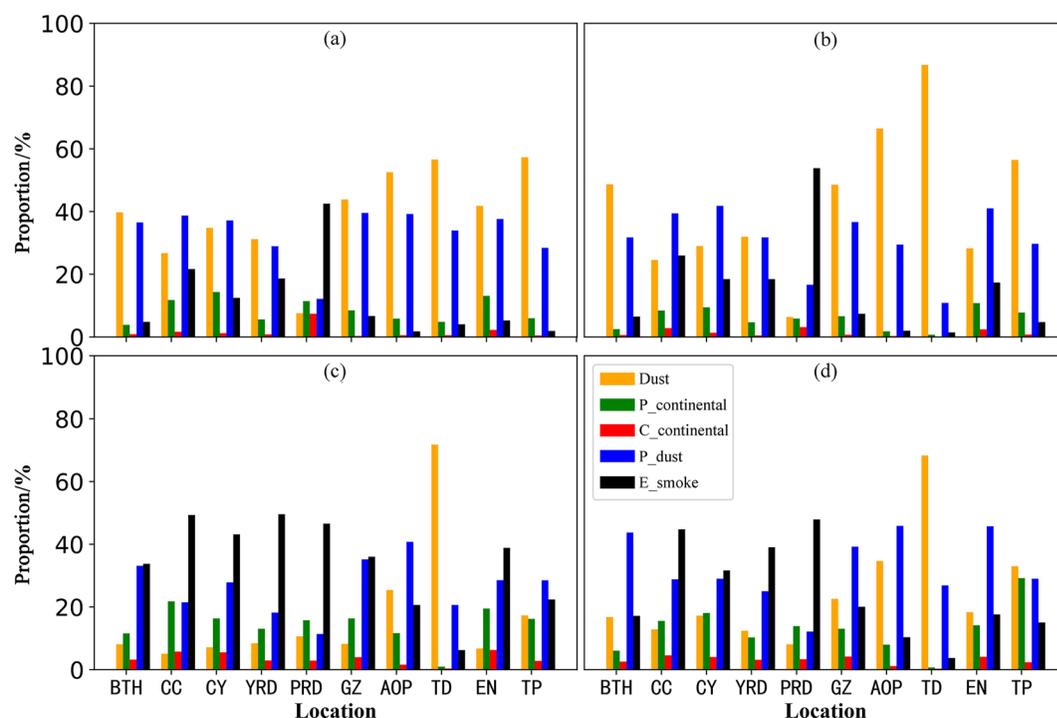
Figure 6. The seasonal average proportion of optical depths of the different aerosol types from June 2006 to December 2020 ((a) winter, (b) spring, (c) summer, (d) autumn).

varied in the different regions, the aerosol trajectory simulation altitude was selected based on the altitude with the maximum frequency of the four aerosol types (dust, polluted dust, polluted continental and elevated smoke aerosols) per year in each region. The HYSPLIT simulation starting time was the time when CALIPSO passed through each region when the four aerosol types were detected.

The backward trajectory clustering results revealed that the TD, as the source region of dust in China, accounted for 82.13% of the total dust aerosols (Figure 7) and 68.36% of the total polluted dust (Figure 8) aerosols in local and surrounding areas (inside the study region, the latitude and longitude of the study region are shown in Table S1 in Supporting Information S1), respectively. Most polluted continental aerosol trajectories originated in Uzbekistan and Urumqi, accounting for 13.79% and 20.44%, of the total trajectories. Elevated smoke aerosols mainly stemmed from the Turan lowlands and Iranian Plateau (Figure S8 in Supporting Information S1). The forward trajectory clustering results demonstrated (Figure S9 in Supporting Information S1) that polluted dust aerosols from the TD region passed through the Alashan and Ordos Plateau region (AOP) and Guanzhong Plain region (GZ) during transport to the east. Dust aerosol trajectories from the TD could reach the AOP, while in AOP region, the trajectories of dust aerosols originating from the direction of northern Xinjiang and Outer Mongolia accounted for 17.35% and 7.94%, respectively, of the total trajectories. Moreover, 28.26% of the polluted continental (Figure S7 in Supporting Information S1) aerosol trajectories stemmed from northern Xinjiang, and 22.88% of the elevated smoke (Figure S8 in Supporting Information S1) aerosol trajectories originated from around Kazakhstan. Dust aerosols stemming from the AOP could reach the GZ and the YRD after being lifted, which resulted in a high frequency of dust aerosols at the 4 km in GZ and the YRD (Figure 3). In addition to dust aerosols from the China's dust source regions, the dust aerosol backward trajectories in the Beijing-Tianjin-Hebei (BTH) and North East China (EN) originated from the direction of the Mongolian Plateau.

The dust (Figure 7) and polluted dust (Figure 8) aerosol trajectories on the TP mainly originated from northern India, the Iranian Plateau and the TD. A total of 40.06% of the dust aerosol trajectories originated from the direction of Nepal and India, and 21.29% of the polluted dust aerosols originated from New Delhi. The trajectories of polluted continental (Figure S7 in Supporting Information S1) and elevated smoke (Figure S8 in Supporting Information S1) aerosols mainly originated from the direction of the Iranian Plateau and northern India. The forward trajectories (Figure S9 in Supporting Information S1) indicated that the four types of aerosols on the TP
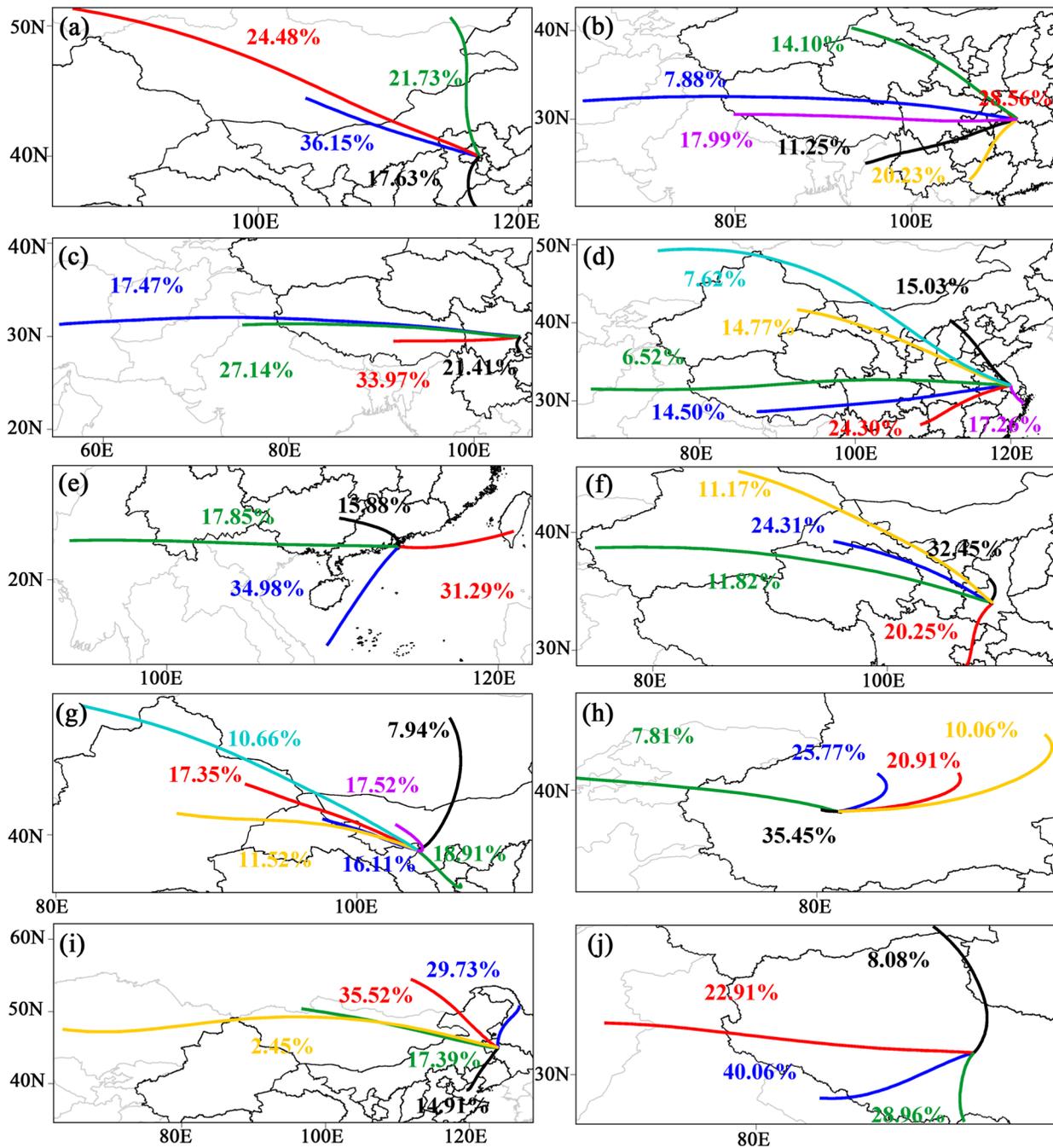
Figure 7. The clustering results for 48 hr backward trajectories of dust aerosol. The numbers (a–j) represent Beijing-Tianjin-Hebei, Central China, Cheng-Yu District, Yangtze River Delta, Pearl River Delta, Guanzhong Plain region, Alashan and Ordos Plateau regionTaklamakan Desert, North East China, and Tibetan Plateau.

were mostly transported to CY District (CY) and GZ, which could lead to the occurrence of dust, polluted dust and elevated smoke aerosols, mainly at altitudes from 2 to 5 km. Moreover, 7.95%, 3.93%, 8.46% and 5.55% of the dust, polluted dust, polluted continental and elevated smoke aerosol trajectories originating from the TP could reach the Northwest Pacific Ocean.

BTH, CC, YRD, PRD, CY, and GZ, the Chinese regions with especially high anthropogenic emissions were associated with polluted continental aerosol trajectories mainly in the local and surrounding areas. The backward trajectory results for the different types of aerosols showed that 36.25% and 37.94% of polluted dust aerosol trajectories (Figure 8) have shorter transmission distances (inside the study region), while 71.44% and 82.74% of
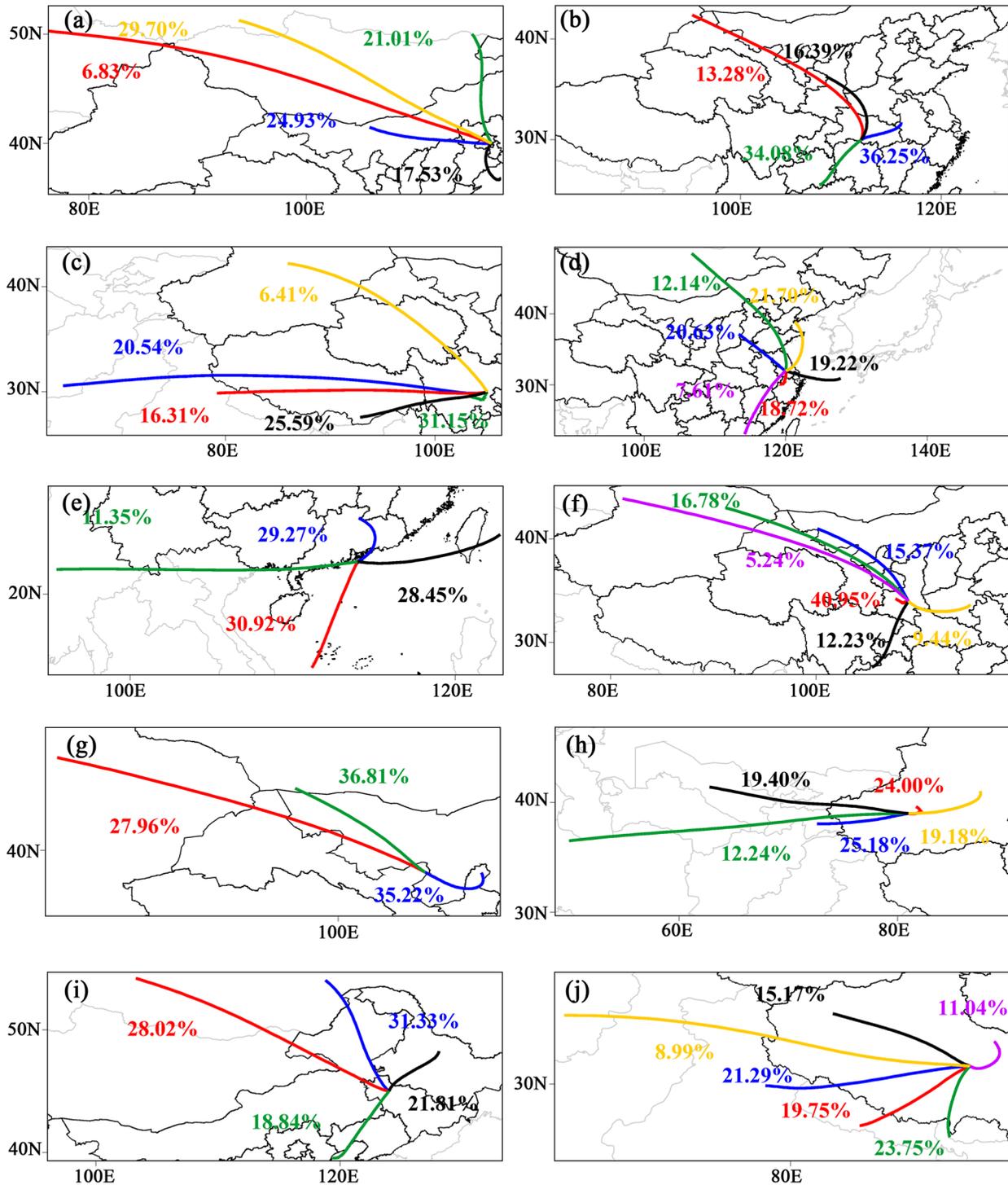
Figure 8. The clustering results for 48 hr backward trajectories of polluted dust aerosol. The numbers (a–j) represent Beijing-Tianjin-Hebei, Central China, Cheng-Yu District, Yangtze River Delta, Pearl River Delta, Guanzhong Plain region, Alashan and Ordos Plateau region, Taklamakan Desert, North East China, and Tibetan Plateau.

dust aerosol trajectories (Figure 7) have longer transmission distances (outside the study region) in the CC and YRD, respectively. This also indicates that the CC and YRD regions have a higher proportion of polluted dust aerosols stemming from local and surrounding areas, while the dust aerosols in these regions mainly originate from long-range aerosol transport. Of the trajectories of polluted dust aerosols in CY, 20.54%, 16.31% and 25.59%

originated from Afghanistan, northern India and the eastern TP, respectively. The forward trajectories (Figure S9 in Supporting Information S1) demonstrated that Korea and Japan exhibited trajectories of polluted continental aerosols from the CC, CY and YRD. Of these, 13.24% of the polluted continental aerosol trajectories from CC reached Korea, and 16.53% of the trajectories from YRD reached Japan. The forward trajectories demonstrated that polluted dust and dust aerosols originating from these regions could be transported to the Northwest Pacific Ocean via Japan. In the PRD, the trajectories of aerosols mainly originated from Southeast Asia. The forward trajectories indicated that 43% of the elevated smoke aerosols could be transported toward the Northwest Pacific Ocean. In EN, 59.35% of the polluted dust aerosols, 49.07% of the polluted continental aerosols, and 46.02% of the elevated smoke aerosols originated from southern Russia and Mongolia, and the most of the aerosols in the EN could be transported through the Sea of Japan to the Northwest Pacific Ocean.

Overall, there was obvious regional variability in the trajectories of the different types of aerosols. To analyze the seasonal differences in the transport process, we clustered the seasonal trajectories of dust, polluted dust, polluted continental and elevated smoke aerosols from 2007 to 2020. The backward trajectories (Figure S10 in Supporting Information S1) indicated that on the TP, the trajectories of dust aerosols from India and Afghanistan in spring, autumn and winter respectively accounted for 76.53%, 78.12%, and 84.8% respectively, of the total trajectories. The forward trajectories demonstrated (Figure S11 in Supporting Information S1) that 33.73% of the AOP dust aerosol trajectories passed through Mongolia, BTH and EN in spring, and the transport distance was relatively short in spring. As a typical transfer region, 66.4% (in spring) and 70.18% (in winter) of the dust aerosol trajectories on the TP reached CY and CC. The transport trajectories were also longer, with 8.97% of the trajectories in spring reaching Japan. According to the backward trajectories of polluted dust aerosols (Figure S12 in Supporting Information S1), the trajectories in BTH and EN originating from Russia and Mongolia in spring accounted for up to 77.23% and 35.25%, respectively, of the total trajectories. The forward trajectories revealed (Figure S13 in Supporting Information S1) that in autumn and winter, 21.67% and 32.46%, respectively, of the trajectories originating in BTH reached the YRD region.

In addition the TP exhibited 65.37% of the polluted continental aerosol trajectories stemming from the direction of India in winter (Figure S14 in Supporting Information S1). Polluted continental aerosols exhibited a longer distance toward the east in BTH and EN in summer, with 3.46% and 7.83%, respectively, of the trajectories reaching the Kuril Islands (Figure S15 in Supporting Information S1). As shown in Figure S16 in Supporting Information S1, the elevated smoke aerosol trajectories in CC mainly originated from Southwest China (30.3% in spring). The percentage of elevated smoke aerosol trajectories stemming from the direction of the Indian Peninsula and Myanmar in CY reached 57.63% in spring. The trajectories of elevated smoke aerosols in the PRD mainly originated from the southwestern direction, accounting for 35.9% of the total trajectories. The forward trajectories indicated (Figure S17 in Supporting Information S1) that the elevated smoke aerosols originating from BTH, EN, CC, PRD, and YRD exhibited long transport distances, with 23.86%, 25.90%, 15.83%, 3.86% and 10.76%, respectively, of the trajectories reaching the Pacific Northwest Ocean in winter.

3.5. Long-Term Trends in Aerosol Transport

To better understand the transport changes among the different aerosol types, the track frequency ($F_{i,j}$, as expressed in formula 1) of the different aerosol types from 2007 to 2020 was calculated. Then, the trend of the annual average track frequency was analyzed using the least squares method. If the trend value is positive, then the forward or backward trajectories passing through a grid point in a given region are increasing, while a negative value indicate the opposite. The results indicated that there were clear geographical differences in the trends of the aerosol trajectories. In the Alashan and Ordos Plateau region (AOP), as a dust source area, the trajectories of dust, polluted dust and polluted continental aerosols from the direction of the Altai Mountains increased. However, the trajectories of dust and elevated smoke aerosols originating from northern Xinjiang clearly decreased (Figure 9), which could influence the weak long-term trend of the dust AOD in the AOP and the observed decrease in the polluted dust AOD (Figure 4). The forward trajectories demonstrated (Figure 10) that the trend of dust and polluted dust aerosol trajectories decreased in the central part of the TD but increased along the southwestern direction, especially polluted dust aerosols, thus explaining the less pronounced trend of the AOD in the TD region (Figure 4). The trends of the polluted continental and dust aerosol trajectories in the TD were the opposite. In addition, the trajectories of elevated smoke aerosols stemming from Turkmenistan and Afghanistan decreased. On the TP, the dust, polluted dust and polluted continental aerosol trajectories stemming from the direction of
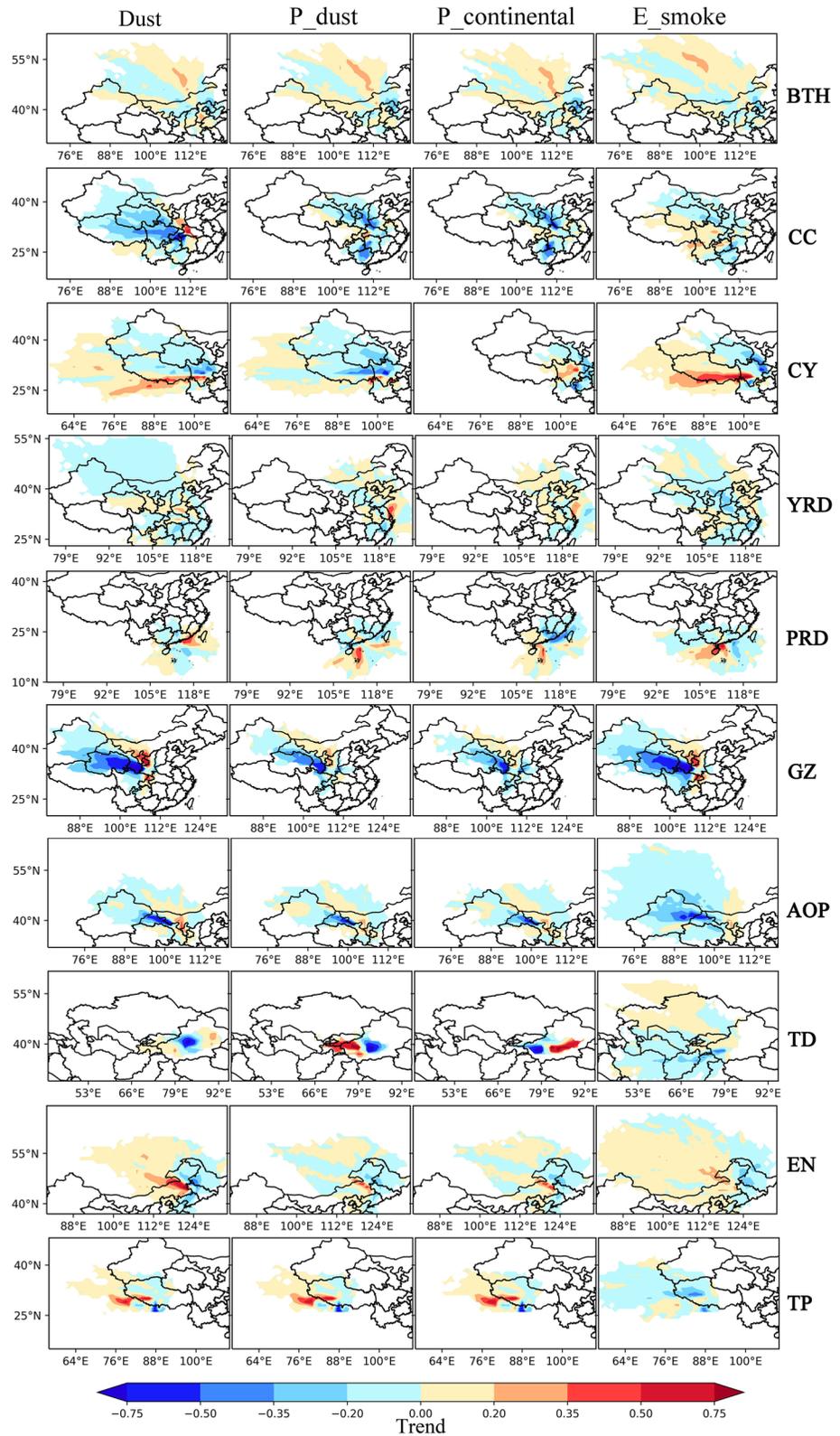
Figure 9. Spatial distribution of the backward trajectory trends of dust aerosol (Column 1), polluted dust aerosol (Column 2), polluted continental aerosol (Column 3), and elevated smoke (Column 4) aerosol in these 10 regions (row). If the trend value is positive, it indicates that trajectories of a region through the grid point is increasing, while a negative value is the opposite.

Figure 10. Spatial distribution of forward trajectory trends of dust aerosol (Column 1), polluted dust aerosol (Column 2), polluted continental aerosol (Column 3), and elevated smoke aerosol (Column 4) in these 10 regions (row). If the trend value is positive, it indicates that trajectories of a region through the grid point is increasing, while a negative value is the opposite.
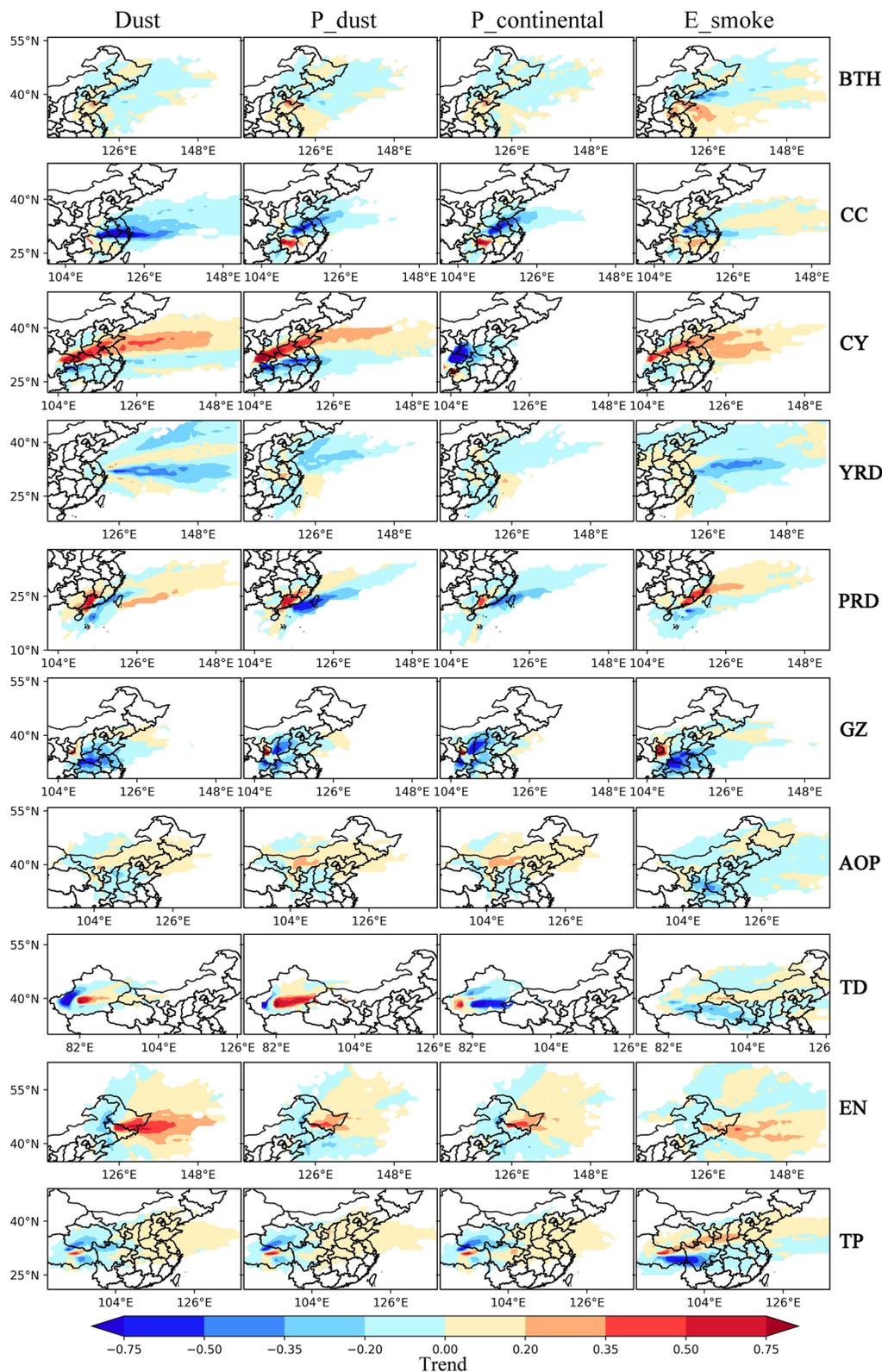
northern India increased. The elevated smoke aerosol trajectories stemming from the direction of Afghanistan and Iran decreased, and the forward trajectories indicated that transport to CY District (CY) and CC decreased.

Aerosol transport from the southern direction of Mongolia toward the Beijing-Tianjin-Hebei (BTH) and North East China (EN) increased, but transport from western Mongolia decreased, with the latter trajectories accounting for a higher proportion of the total trajectories (as shown in Figure 7). The forward trajectories (Figure 10) demonstrated that the trajectories of dust and polluted dust aerosols in BTH and EN originating from the AOP increased, while the AOD of dust aerosols in EN increased. The elevated smoke aerosol trajectories stemming from the westward direction in CC, such as the TP and Yunnan-Guizhou regions, increased, while the trajectories of dust, polluted dust and polluted continental aerosols from the northwest and west directions decreased. As a result, the AOD of polluted dust and polluted continental aerosols decreased.

Based on the forward trajectory trends (Figure 10), the aerosol transport from Guanzhong Plain region (GZ) and CC to the PRD decreased. The dust and polluted dust aerosol trajectories from Xinjiang and Qinghai decreased in CY, and the dust aerosol trajectories stemming from the direction of the Thar Desert and elevated smoke aerosol trajectories stemming from Afghanistan and India increased. However, the polluted dust aerosol trajectories mostly decreased, which may be attributed to the decrease in the AOD of polluted dust aerosols in CY. In the PRD, the dust and elevated smoke aerosol trajectories originating from the southwestern regions increased, but the local elevated smoke AOD decreased, which is consistent with the decrease in the PRD. Based on the forward trajectories (Figure 10), the transport of dust, polluted dust and elevated smoke aerosols from CY and PRD to the Northwest Pacific Ocean significantly increased.

4. Discussion and Conclusion

Based on CALIOP data from June 2006 to December 2020, this study analyzed the changes the vertical structure and seasonal distribution of various aerosol types in typical regions of China. Furthermore, the long-term trends of the AOD were assessed. Finally, the HYSPLIT model was used to obtain the transport paths of aerosols in the different regions and to analyze the trends of aerosol trajectories. The results indicated the following.

1. The vertical distribution of aerosols in China revealed significant geographical and seasonal variabilities. The highest AEC was observed in CC and Guanzhong Plain region (GZ). The high AEC (>0.35 km^{-1}) at altitudes ranging from 0 to 2 km could be mainly attributed to polluted dust and polluted continental aerosols, with aerosols dominated by more regularly shaped fine particles, especially in winter, followed by autumn. In the TD, high AEC values (>0.2 km^{-1}) were distributed from 1 to 3 km, and were mainly associated with dust aerosols, with the greatest contribution in spring, and aerosols were dominated by more irregular coarse particles. The TP accounted for the lowest AEC, higher values (>0.1 km^{-1}) associated mainly with dust and polluted dust aerosols were distributed at altitudes from 4 to 5 km, and the seasonal variability was low.

2. There were significant differences in the distribution of the AOD and its trends in China. High AOD values in China were distributed in North China, CC, and South China, where anthropogenic activities were more frequent. Low AOD values mainly occurred on the TP. The dust AOD was the highest in the TD region, high values of the polluted dust AOD values were distributed in North China and CC, and high values of the elevated smoke AOD values were distributed in South China. The trends of the long-term AOD were found to be significantly decreased in all regions except the TD and TP, where the trends were not significant. The AOD trend in the study region was clearly influenced by the dominant aerosol type and the altitude of high AOD. In the TD region at approximately 2 km, the occurrence frequency of dust aerosols reached 35%, influenced by 2–4 km dust aerosols, resulting in a weaker AOD trend. However, the AOD trend in the TP region was mainly influenced by 4–8 km aerosols and polluted dust aerosols. In the YRD and North East China (EN) regions, the 0–2 km AOD and polluted dust AOD values exhibited significant decreases, and although the polluted continental AOD increased, the highest frequency of polluted dust aerosols occurred below 4 km, so the AOD in the YRD and EN regions revealed a significant decrease.

3. The reduction in the AOD is due not only due to the influence of local emissions, but also to the influence of long-range transport aerosols on the composition and optical properties in the 10 regions. There were significant regional differences between the transport trajectories of the four types of aerosols (dust aerosols, polluted dust aerosols, polluted continental aerosols, and elevated smoke aerosols). In addition to the contribution of dust aerosol transport from China's dust source areas, cross-border transport occurred from dust aerosol source areas outside of China. For example, 57.88% and 55.36% of the dust aerosol trajectories in the

BTH and EN region, respectively, originated from the Mongolian Plateau. Dust transport from the Mongolian Plateau is increasing in the EN region, which may be affected by the dust aerosol transport from the Mongolian Plateau. In addition, the dust aerosol trajectories on the TP mainly originated from India, Afghanistan and the TD region, with the backward trajectories exhibiting an increasing trend. The PRD was dominated by elevated smoke aerosols, with trajectories mainly originating from the direction of Myanmar and Vietnam, accounting for 27.38% and 29.59%, respectively, of the total trajectories. The trajectories revealed both increasing (Vietnam) and decreasing (Myanmar) trends, which resulted in a lower trend of the elevated smoke AOD variability in the PRD region.

During the long-range transport of aerosols, the deposition and uplift of aerosols are influenced by the topography and local weather circulation (Iwasaka et al., 1983; Sun et al., 2000; Tsai et al., 2008; Zhao et al., 2010). The vertical distribution of aerosols is also affected by their source location and seasons (Alpert et al., 2004; Liu et al., 2012). The dust aerosols from Mongolia and the Gobi Desert in China do not reach altitudes greater than 3 km (Sun et al., 2001), whereas dust from the TD can be lifted up to 8 km (Chen, Song, Huang, et al., 2022; Huang et al., 2008). Areas with many anthropogenic pollution sources, such as the PRD, YRD, and CC, were dominated by polluted continental aerosols and polluted dust aerosols below 2 km, mainly resulting from the local and industrial emissions in the surrounding areas. These aerosols were transported to South Korea, Japan, and even the Northwest Pacific Ocean and the Sea of Okhotsk. These aerosols resulting from industrial emissions not only threaten the air quality in local and transported areas (Choel et al., 2010; Ma et al., 2018; Sun et al., 2018; Wang & Hao, 2012) but also affect regional and global climate conditions (Popovicheva et al., 2021; Zhang et al., 2018). In the long-range transport process of aerosols, the mechanisms affecting the vertical distribution and transport path changes of the different aerosol types, as well as the impact on the environment and climate, will be examined in future work from the perspective of multiscale atmospheric physical processes.

Conflict of Interest

The authors declare no conflicts of interest relevant to this study.

Data Availability Statement

Cloud-Aerosol Lidar with Orthogonal Polarization data can be download from the NASA Langley ASDC center, https://subset.larc.nasa.gov/calipso/login.php (CALIOP, 2022). Global data assimilation and prediction system (GDAS) data set can be obtained online (https://www.ready.noaa.gov/data/archives/gdas1).

References

Abdalmogith, S. S., & Harrison, R. M. (2005). The use of trajectory cluster analysis to examine the long-range transport of secondary inorganic aerosol in the UK. *Atmospheric Environment*, *39*(35), 6686–6695. https://doi.org/10.1016/j.atmosenv.2005.07.059

Alpert, P., Kishcha, P., Shtivelman, A., Krichak, S. O., & Joseph, J. H. (2004). Vertical distribution of Saharan dust based on 2.5-year model predictions. *Atmospheric Research*, *70*(2), 109–130. https://doi.org/10.1016/j.atmosres.2003.11.001

Amiridis, V., Giannakaki, E., Balis, D. S., Gerasopoulos, E., Pytharoulis, I., Zanis, P., et al. (2010). Smoke injection heights from agricultural burning in Eastern Europe as seen by Calipso. *Atmospheric Chemistry and Physics*, *10*(23), 11567–76. https://doi.org/10.5194/acp-10-11567-2010

Andreae, M. O., Berresheim, H., Andreae, T. W., Kritz, M. A., Bates, T. S., & Merrill, J. T. (1988). Vertical-distribution of dimethylsulfide, sulfur-dioxide, aerosol ions, and Radon over the Northeast Pacific-Ocean. *Journal of Atmospheric Chemistry*, *6*(1–2), 149–173. https://doi.org/10.1007/bf00048337

Babu, C. A., & Sivaprasad, P. (2014). Variability and mechanisms of vertical distribution of aerosols over the Indian region. *International Journal of Remote Sensing*, *35*(22), 7691–7705. https://doi.org/10.1080/01431161.2014.975379

Borge, R., Lumbreras, J., Vardoulakis, S., Kassomenos, P., & Rodriguez, E. (2007). Analysis of long-range transport influences on urban Pm10 using two-stage atmospheric trajectory clusters. *Atmospheric Environment*, *41*(21), 4434–4450. https://doi.org/10.1016/j.atmosenv.2007.01.053

Brakhasi, F., Hajeb, M., Mielonen, T., Matkan, A., & Verbesselt, J. (2021). Investigating aerosol vertical distribution using Calipso time series over the Middle East and North Africa (Mena), Europe, and India: A Bfast-based gradual and abrupt change detection. *Remote Sensing of Environment*, *264*, 112619. https://doi.org/10.1016/j.rse.2021.112619

CALIOP (2022). CALIOP. [Dataset]. Retrieved from https://subset.larc.nasa.gov/calipso/login.php

Cao, G. L., Zhang, X. Y., Wang, Y. Q., & Zheng, F. C. (2008). Estimation of emissions from field burning of crop straw in China. *Chinese Science Bulletin*, *53*(5), 784–790. https://doi.org/10.1007/s11434-008-0145-4

Charlson, R. J., Schwartz, S. E., Hales, J. M., Cess, R. D., Coakley, J. A., Hansen, J. E., & Hofmann, D. J. (1992). Climate forcing by anthropogenic aerosols. *Science*, *255*(5043), 423–430. https://doi.org/10.1126/science.255.5043.423

Che, H., Xia, X., Zhu, J., Wang, H., Wang, Y., Sun, J., et al. (2015). Aerosol optical properties under the condition of Heavy Haze over an urban site of Beijing, China. *Environmental Science & Pollution Research*, *22*(2), 1043–1053. https://doi.org/10.1007/s11356-014-3415-5

Chen, B., Huang, Y., Huang, J., Dong, L., Guan, X., Ge, J., & Hu, Z. (2021). Using lidar and historical similar meteorological fields to evaluate the impact of anthropogenic control on dust weather during Covid-19. *Frontiers in Environmental Science*, *9*, 16. https://doi.org/10.3389/fenvs.2021.806094

Chen, B., Song, Z., Huang, J., Zhang, P., Hu, X., Zhang, X., et al. (2022). Estimation of Atmospheric PM10 concentration in China using an interpretable deep learning model and top-of-the-atmosphere reflectance data from China's new generation geostationary meteorological satellite, FY-4A. *Journal of Geophysical Research-Atmosphere*, *127*(9), e2021JD036393. https://doi.org/10.1029/2021JD036393

Chen, B., Song, Z., Shi, B., & Li, M. (2022a). An interpretable deep forest model for estimating hourly Pm 10 concentration in China using Himawari-8 data. *Atmospheric Environment*, *268*, 118827. https://doi.org/10.1016/j.atmosenv.2021.118827

Chen, W. T., Liao, H., & Seinfeld, J. H. (2007). Future climate impacts of direct radiative forcing of anthropogenic aerosols, tropospheric ozone, and long-lived greenhouse gases. *Journal of Geophysical Research*, *112*(D14), D14209. https://doi.org/10.1029/2006jd008051

Chen, Y. H., Liu, Q., Geng, F. H., Zhang, H., Cai, C. J., Xu, T. T., et al. (2012). Vertical distribution of optical and Micro-physical properties of ambient aerosols during Dry Haze periods in Shanghai. *Atmospheric Environment*, *50*, 50–59. https://doi.org/10.1016/j.atmosenv.2012.01.002

Choel, M., Deboudt, K., & Flament, P. (2010). Development of time-resolved description of aerosol properties at the particle scale during an episode of industrial pollution plume. *Water, Air, and Soil Pollution*, *209*(1–4), 93–107. https://doi.org/10.1007/s11270-009-0183-9

Chung, C. E., Ramanathan, V., Kim, D., & Podgorny, I. A. (2005). Global anthropogenic aerosol direct forcing derived from satellite and ground-based observations. *Journal of Geophysical Research*, *110*(D24), D24207. https://doi.org/10.1029/2005jd006356

Cohen, M., Artz, R., Draxler, R., Miller, P., Poissant, L., Niemi, D., et al. (2004). Modeling the atmospheric transport and deposition of Mercury to the great lakes. *Environmental Research*, *95*(3), 247–265. https://doi.org/10.1016/j.envres.2003.11.007

Ding, K., Huang, X., Ding, A. J., Wang, M. H., Su, H., Kerminen, V. M., et al. (2021). Aerosol-boundary-layer-monsoon interactions amplify semi-direct effect of biomass smoke on low cloud formation in Southeast Asia. *Nature Communications*, *12*(1), 6416. https://doi.org/10.1038/s41467-021-26728-4

Dong, L., Chen, B., Huang, Y., Song, Z., & Yang, T. J. A. (2021). Analysis on the characteristics of air pollution in China during the Covid-19 outbreak. *Atmosphere*, *12*(2), 205. https://doi.org/10.3390/ATMOS12020205

Dorling, S. R., Davies, T. D., & Pierce, C. E. (1992). Cluster-analysis - a technique for estimating the synoptic meteorological controls on air and precipitation Chemistry - results from Eskdalemuir, South Scotland. *Atmospheric Environment, Part A: General Topics*, *26*(14), 2583–2602. https://doi.org/10.1016/0960-1686(92)90111-w

Draxler, R., Arnold, D., Chino, M., Galmarini, S., Hort, M., Jones, A., et al. (2015). World Meteorological Organization's model simulations of the radionuclide dispersion and deposition from the Fukushima Daiichi nuclear power plant accident. *Journal of Environmental Radioactivity*, *139*, 172–184. https://doi.org/10.1016/j.jenvrad.2013.09.014

Draxler, R. R. (2003). Hysplit (Hybrid Single-Particle Lagrangian Integrated Trajectory) Model Access Via Noaaarl Ready Website. Retrieved from http://www.arl.noaa.gov/ready/hysplit4.html

Draxler, R. R., & Hess, G. D. (1997). Description of the Hysplit_4 modeling system.

Draxler, R. R., & Hess, G. D. (1998). An overview of the Hysplit_4 modelling system for trajectories, dispersion and deposition. *Australian Meteorological Magazine*, *47*, 295–308.

Fleming, Z. L., Monks, P. S., & Manning, A. J. (2012). Review: Untangling the influence of air-mass history in interpreting observed atmospheric composition. *Atmospheric Research*, *104*, 1–39. https://doi.org/10.1016/j.atmosres.2011.09.009

Fridlind, A. M., Ackerman, A. S., Jensen, E. J., Heymsfield, A. J., Poellot, M. R., Stevens, D. E., et al. (2004). Evidence for the predominance of mid-tropospheric aerosols as subtropical anvil cloud nuclei. *Science*, *304*(5671), 718–722. https://doi.org/10.1126/science.1094947

Ganguly, D., Rasch, P. J., Wang, H. L., & Yoon, J. H. (2012). Fast and slow Responses of the South Asian monsoon system to anthropogenic aerosols. *Geophysical Research Letters*, *39*(18). https://doi.org/10.1029/2012gl053043

Gui, K., Che, H. Z., Zheng, Y., Zhao, H. J., Yao, W. R., Li, L., et al. (2021). Three-dimensional climatology, trends, and meteorological drivers of global and regional tropospheric type-dependent aerosols: Insights from 13 Years (2007-2019) of Caliop observations. *Atmospheric Chemistry and Physics*, *21*(19), 15309–15336. https://doi.org/10.5194/acp-21-15309-2021

Han, Y., Wang, T. H., Tang, J. Y., Wang, C. Y., Jian, B. D., Huang, Z. W., & Huang, J. (2022). New insights into the Asian dust cycle derived from Calipso lidar measurements. *Remote Sensing of Environment*, *272*, 112906. https://doi.org/10.1016/j.rse.2022.112906

He, J., Gong, S., Yu, Y., Yu, L., Wu, L., Mao, H., et al. (2017). Air pollution characteristics and their relation to meteorological conditions during 2014-2015 in Major Chinese Cities. *Environmental Pollution*, *223*, 484–496. https://doi.org/10.1016/j.envpol.2017.01.050

Huang, J., Minnis, P., Chen, B., Huang, Z. W., Liu, Z. Y., Zhao, Q. Y., et al. (2008). Long-range transport and vertical structure of Asian dust from Calipso and surface measurements during Pacdex. *Journal of Geophysical Research*, *113*(D23), D23212. https://doi.org/10.1029/2008jd010620

Huang, J. P., Liu, J. J., Chen, B., & Nasiri, S. L. (2015). Detection of anthropogenic dust using Calipso lidar measurements. *Atmospheric Chemistry and Physics*, *15*(20), 11653–11665. https://doi.org/10.5194/acp-15-11653-2015

Huang, J. P., Minnis, P., Yi, Y. H., Tang, Q., Wang, X., Hu, Y. X., et al. (2007). Summer dust aerosols detected from Calipso over the Tibetan plateau. *Geophysical Research Letters*, *34*(18), L18805. https://doi.org/10.1029/2007gl029938

Iwasaka, Y., Minoura, H., & Nagaya, K. (1983). The transport and spacial scale of Asian dust-storm clouds - A Case-study of the dust-storm event of April 1979. *Tellus Series B Chemical and Physical Meteorology*, *35*(3), 189–196. https://doi.org/10.1111/j.1600-0889.1983.tb00023.x

Jiang, J. H., Su, H., Huang, L., Wang, Y., Massie, S., Zhao, B., et al. (2018). Contrasting effects on deep convective clouds by different types of aerosols. *Nature Communications*, *9*(1), 3874. https://doi.org/10.1038/s41467-018-06280-4

Kim, D., Chin, M., Cruz, C. A., Tong, D., & Yu, H. B. (2021). Spring dust in Western North America and its interannual variability-understanding the role of local and transported dust. *Journal of Geophysical Research: Atmosphere*, *126*(22). https://doi.org/10.1029/2021jd035383

Kim, M. H., Omar, A. H., Tackett, J. L., Vaughan, M. A., Winker, D. M., Trepte, C. R., et al. (2018). The Calipso version 4 automated aerosol classification and lidar ratio selection algorithm. *Atmospheric Measurement Techniques*, *11*, 6107–6135. https://doi.org/10.5194/amt-11-6107-2018

Koren, I., Kaufman, Y. J., Remer, L. A., & Martins, J. V. (2004). Measurement of the effect of amazon smoke on inhibition of cloud formation. *Science*, *303*(5662), 1342–1345. https://doi.org/10.1126/science.1089424

Lakshmi, N. B., Nair, V. S., & Babu, S. S. (2021). Assessment of the vertical distribution of speciated aerosol absorption over South Asia using spaceborne lidar and ground-based observations. *Remote Sensing of Environment*, *253*, 112164. https://doi.org/10.1016/j.rse.2020.112164

Lebo, Z. J. (2014). The sensitivity of a numerically simulated idealized squall line to the vertical distribution of aerosols. *Journal of the Atmospheric Sciences*, *71*(12), 187–202. https://doi.org/10.1175/jas-d-14-0068.1

Li, J. X., Liu, X. G., Yuan, L., Yin, Y., Li, Z. Q., Li, P. R., et al. (2015). Vertical distribution of aerosol optical properties based on aircraft measurements over the Loess plateau in China. *Journal of Environmental Sciences*, *34*, 44–56. https://doi.org/10.1016/j.jes.2015.01.021

Liu, D., Wang, Y. J., Wang, Z., & Zhou, J. (2012). The three-dimensional structure of transatlantic African dust transport: A new perspective from Calipso lidar measurements. *Advances in Meteorology*, *2012*, 1–9. https://doi.org/10.1155/2012/850704

Liu, Y. Q., Lin, T., Hong, J., Wang, Y. H., Shi, L. M., Huang, Y. Y., et al. (2021). Multi-dimensional satellite observations of aerosol properties and aerosol types over three Major urban clusters in Eastern China. *Atmospheric Chemistry and Physics*, *21*(16), 12331–12358. https://doi.org/10.5194/acp-21-12331-2021

Liu, Z., Liu, D., Huang, J., Vaughan, M., Uno, I., Sugimoto, N., et al. (2008). Airborne dust distributions over the Tibetan plateau and surrounding areas derived from the first year of Calipso lidar observations. *Atmospheric Chemistry and Physics*, *8*(16), 5045–5060. https://doi.org/10.5194/acp-8-5045-2008

Liu, Z. Y., Vaughan, M., Winker, D., Kittaka, C., Getzewich, B., Kuehn, R., et al. (2009). The Calipso lidar cloud and aerosol discrimination: Version 2 algorithm and initial assessment of performance. *Journal of Atmospheric and Oceanic Technology*, *26*(7), 1198–1213. https://doi.org/10.1175/2009jtecha1229.1

Ma, X., Jia, H., Yu, F., & Quaas, J. (2018). Opposite aerosol index-cloud droplet effective radius correlations over major industrial regions and their adjacent oceans. *Geophysical Research Letters*, *45*(11), 5771–5778. https://doi.org/10.1029/2018gl077562

Ma, X. Y., & Yu, F. Q. (2014). Seasonal variability of aerosol vertical profiles over East US and West Europe: Geos-Chem/Apm simulation and comparison with Calipso observations. *Atmospheric Research*, *140*, 28–37. https://doi.org/10.1016/j.atmosres.2014.01.001

Marinescu, P. J., van den Heever, S. C., Saleeby, S. M., Kreidenweis, S. M., & DeMott, P. J. (2017). The microphysical roles of lower-tropospheric versus midtropospheric aerosol particles in mature-stage MCS precipitation. *Journal of the Atmospheric Sciences*, *74*(11), 3657–3678. https://doi.org/10.1175/jas-d-16-0361.1

McKendry, I., Strawbridge, K., Karumudi, M. L., O'Neill, N., Macdonald, A. M., Leaitch, R., et al. (2011). Californian forest fire plumes over Southwestern British Columbia: Lidar, sunphotometry, and mountaintop chemistry observations. *Atmospheric Chemistry and Physics*, *11*(2), 465–477. https://doi.org/10.5194/acp-11-465-2011

Mehta, M., Khushboo, R., Raj, R., & Singh, N. (2021). Spaceborne observations of aerosol vertical distribution over Indian mainland (2009-2018). *Atmospheric Environment*, *244*, 117902. https://doi.org/10.1016/j.atmosenv.2020.117902

Mehta, M., Singh, N., & Anshumali (2018). Global trends of columnar and vertically distributed properties of aerosols with emphasis on dust, polluted dust and smoke - inferences from 10-year long Caliop observations. *Remote Sensing of Environment*, *208*, 120–132. https://doi.org/10.1016/j.rse.2018.02.017

Mishra, A. K., & Shibata, T. (2012). Climatological aspects of seasonal variation of aerosol vertical distribution over Central Indo-Gangetic Belt (IGB) inferred by the space-borne lidar Caliop. *Atmospheric Environment*, *46*, 365–375. https://doi.org/10.1016/j.atmosenv.2011.09.052

Muller, D., Mattis, I., Wandinger, U., Ansmann, A., Althausen, D., Dubovik, O., et al. (2003). Saharan dust over a Central European Earlinet-Aeronet site: Combined observations with Raman lidar and Sun photometer. *Journal of Geophysical Research*, *108*(D12), 4345. https://doi.org/10.1029/2002jd002918

Omar, A. H., Winker, D. M., Kittaka, C., Vaughan, M. A., Liu, Z. Y., Hu, Y. X., et al. (2009). The Calipso automated aerosol classification and lidar ratio selection algorithm. *Journal of Atmospheric and Oceanic Technology*, *26*(10), 1994–2014. https://doi.org/10.1175/2009jtecha1231.1

Ou, J., Meng, J., Zheng, J., Mi, Z., Bian, Y., Yu, X., et al. (2017). Demand-driven air pollutant emissions for a fast-developing region in China. *Applied Energy*, *204*, 131–142. https://doi.org/10.1016/j.apenergy.2017.06.112

Popovicheva, O., Molozhnikova, E., Nasonov, S., Potemkin, V., Penner, I., Klemasheva, M., et al. (2021). Industrial and wildfire aerosol pollution over world heritage Lake Baikal. *Journal of Environmental Sciences*, *107*, 49–64. https://doi.org/10.1016/j.jes.2021.01.011

Ramanathan, V., Crutzen, P. J., Kiehl, J. T., & Rosenfeld, & D. (2001). Aerosols, climate, and the hydrological cycle. *Science*, *294*(5549), 2119–2124. https://doi.org/10.1126/science.106403

Ramanathan, V., & Feng, Y. (2009). Air pollution, greenhouse gases and climate change: Global and regional perspectives. *Atmospheric Environment*, *43*(1), 37–50. https://doi.org/10.1016/j.atmosenv.2008.09.063

Ratnam, M. V., Prasad, P., Raj, S. T. A., Raman, M. R., & Basha, G. (2021). Changing patterns in aerosol vertical distribution over South and East Asia. *Scientific Reports*, *11*(1), 308. https://doi.org/10.1038/s41598-020-79361-4

Rosenfeld, D., Lohmann, U., Raga, G. B., O'Dowd, C. D., Kulmala, M., Fuzzi, S., et al. (2008). Flood or drought: How do aerosols affect precipitation? *Science*. https://doi.org/10.1126/science.1160606

Shen, J., & Cao, N. W. (2020). Comprehensive observation and analysis of aerosol optical properties and vertical distribution in Nanjing, China. *Atmospheric Environment*, *239*, 117767. https://doi.org/10.1016/j.atmosenv.2020.117767

Shimizu, A., Sugimoto, N., Matsui, I., Arao, K., Uno, I., Murayama, T., et al. (2004). Continuous observations of Asian dust and other aerosols by polarization lidars in China and Japan during ACE-Asia. *Journal of Geophysical Research*, *109*(D19), D19S17. https://doi.org/10.1029/2002jd003253

Srinivas, C. V., Venkatesan, R., Baskaran, R., Rajagopal, V., & Venkatraman, B. (2012). Regional scale atmospheric dispersion simulation of accidental releases of radionuclides from Fukushima Dai-Ichi Reactor. *Atmospheric Environment*, *61*, 66–84. https://doi.org/10.1016/j.atmosenv.2012.06.082

Stein, A. F., Draxler, R. R., Rolph, G. D., Stunder, B. J. B., Cohen, M. D., & Ngan, F. (2015). Noaa'srjrplit atmospheric transport and dispersion modeling system. *Bulletin of the American Meteorological Society*, *96*(12), 2059–2077. https://doi.org/10.1175/bams-d-14-00110.1

Su, L., Yuan, Z. B., Fung, J. C. H., & Lau, A. K. H. (2015). A comparison of hysplit backward trajectories generated from two GDAS datasets. *Science of the Total Environment*, *506*, 527–537. https://doi.org/10.1016/j.scitotenv.2014.11.072

Sun, J. M., Liu, T. S., & Lei, Z. F. (2000). Sources of heavy dust fall in Beijing, China on April 16, 1998. *Geophysical Research Letters*, *27*(14), 2105–2108. https://doi.org/10.1029/1999gl010814

Sun, J. M., Zhang, M. Y., & Liu, T. S. (2001). Spatial and temporal characteristics of dust storms in China and its surrounding regions, 1960-1999: Relations to source area and climate. *Journal of Geophysical Research*, *106*(D10), 10325–10333. https://doi.org/10.1029/2000jd900665

Sun, L., Li, R. B., Tian, X. P., & Wei, J. (2017). Analysis of the temporal and spatial variation of aerosols in the Beijing-Tianjin-Hebei region with a 1 Km AOD product. *Aerosol and Air Quality Research*, *17*(3), 923–935. https://doi.org/10.4209/aaqr.2016.05.0185

Sun, T., Che, H., Qi, B., Wang, Y., Dong, Y., Xia, X., et al. (2018). Aerosol optical characteristics and their vertical distributions under enhanced haze pollution events: Effect of the regional transport of different aerosol types over eastern China. *Atmospheric Chemistry and Physics*, *18*(4), 2949–2971. https://doi.org/10.5194/acp-18-2949-2018

Sun, X. Y., Zhao, T. L., Bai, Y. Q., Kong, S. F., Zheng, H., Hu, W. Y., et al. (2022). Meteorology impact on PM2.5 change over a receptor region in the regional transport of air pollutants: Observational study of recent emission reductions in central China. *Atmospheric Chemistry and Physics*, *22*(5), 3579–3593. https://doi.org/10.5194/acp-22-3579-2022

Tsai, F., Chen, G. T. J., Liu, T. H., Lin, W. D., & Tu, J. Y. (2008). Characterizing the transport pathways of Asian dust. *Journal of Geophysical Research*, *113*(D17), D17311. https://doi.org/10.1029/2007jd009674

VanCuren, R. A. (2003). Asian aerosols in North America: Extracting the chemical composition and mass concentration of the Asian continental aerosol plume from long-term aerosol records in the Western United States. *Journal of Geophysical Research*, *108*(D20), 4623. https://doi.org/10.1029/2003jd003459

Veal, A. J. (2021). Climate change 2021: The physical science basis, 6th report. *World Leisure Journal*, *63*(4), 443–444. https://doi.org/10.1080/16078055.2021.2008646

Wang, H., Sun, Z. B., Li, H. Y., Gao, Y., Wu, J., & Cheng, T. T. (2018). Vertical-distribution characteristics of atmospheric aerosols under different thermodynamic conditions in Beijing. *Aerosol and Air Quality Research*, *18*(11), 2775–2787. https://doi.org/10.4209/aaqr.2018.03.0078

Wang, S., & Hao, J. (2012). Air quality management in China: Issues, challenges, and options. *Journal of Environmental Sciences*, *24*(1), 2–13. https://doi.org/10.1016/s1001-0742(11)60724-9

Wang, W. C., Huang, J. P., Minnis, P., Hu, Y. X., Li, J. M., Huang, Z. W., et al. (2010). Dusty cloud properties and radiative forcing over dust source and downwind regions derived from a-train data during the Pacific dust experiment. *Journal of Geophysical Research*, *115*, D00H35. https://doi.org/10.1029/2010jd014109

Wang, W. C., Sheng, L. F., Jin, H. C., & Han, Y. Q. (2015). Dust aerosol effects on cirrus and altocumulus clouds in Northwest China. *J. Meteorol. Res.*, *29*(5), 793–805. https://doi.org/10.1007/s13351-015-4116-9

Winker, D., Hostetler, C., & Hunt, W. (2004). CALIOP: The CALIPSO lidar. In *Proceedings of 22nd International Laser Radar Conference (ESASP 561). Matera, Italy* (pp. 941–944).

Winker, D. M., Hunt, W., & Hostetler, C. (2004). Status and performance of the Caliop lidar. *Laser Radar Techniques for Atmospheric Sensing*, *5575*, 8–15. https://doi.org/10.1117/12.571955

Winker, D. M., Hunt, W. H., & McGill, M. J. (2007). Initial performance assessment of Caliop. *Geophysical Research Letters*, *34*(19), L19803. https://doi.org/10.1029/2007gl030135

Winker, D. M., Tackett, J. L., Getzewich, B. J., Liu, Z., Vaughan, M. A., & Rogers, R. R. (2013). The global 3-D distribution of tropospheric aerosols as characterized by Caliop. *Atmospheric Chemistry and Physics*, *13*(6), 3345–3361. https://doi.org/10.5194/acp-13-3345-2013

Winker, D. M., Vaughan, M., & Hunt, W. (2006). The CALIPSO mission and initial results from CALIOP. *Proceedings of SPIE*, 6409. https://doi.org/10.1117/12.698003

Yang, W., Marshak, A., Varnai, T., Kalashnikova, O. V., & Kostinski, A. B. (2012). Calipso observations of transatlantic dust: Vertical stratification and effect of clouds. *Atmospheric Chemistry and Physics*, *12*(23), 11339–11354. https://doi.org/10.5194/acp-12-11339-2012

Yang, Y. K., Zhao, C. F., Wang, Q., Cong, Z. Y., Yang, X. C., & Fan, H. (2021). Aerosol characteristics at the three poles of the Earth as characterized by cloud-aerosol lidar and infrared pathfinder satellite observations. *Atmospheric Chemistry and Physics*, *21*(6), 4849–4868. https://doi.org/10.5194/acp-21-4849-2021

Young, S. A., Vaughan, M. A., Garnier, A., Tackett, J. L., Lambeth, J. D., & Powell, K. A. (2018). Extinction and optical depth Retrievals for Calipso's version 4 data release. *Atmospheric Measurement Techniques*, *11*(10), 5701–5727. https://doi.org/10.5194/amt-11-5701-2018

Yu, S. Q., Liu, D., Xu, J. W., Wang, Z. Z., Wu, D. C., Shan, Y. P., et al. (2021). Optical properties and seasonal distribution of aerosol layers observed by lidar over Jinhua, Southeast China. *Atmospheric Environment*, *257*, 118456. https://doi.org/10.1016/j.atmosenv.2021.118456

Yuan, T. G., Chen, S. Y., Huang, J. P., Wu, D. Y., Lu, H., Zhang, G. L., et al. (2019). Influence of dynamic and thermal forcing on the meridional transport of Taklimakan Desert dust in spring and summer. *Journal of Climate*, *32*(3), 749–767. https://doi.org/10.1175/jcli-d-18-0361.1

Zhang, K., Ma, Y., Xin, J., Liu, Z., Ma, Y., Gao, D., et al. (2018). The aerosol optical properties and PM2.5 components over the world's largest industrial zone in Tangshan, North China. *Atmospheric Research*, *201*, 226–234. https://doi.org/10.1016/j.atmosres.2017.10.025

Zhang, K. Y., Zhao, C. F., Fan, H., Yang, Y. K., & Sun, Y. (2020). Toward understanding the differences of Pm(2.5)Characteristics among five China urban Cities. *Asia-Pacific J. Atmos. Sci.*, *56*(4), 493–502. https://doi.org/10.1007/s13143-019-00125-w

Zhang, M. Z., Deng, X., Zhu, R. H., Ren, Y. Z., & Xue, H. W. (2021). The impact of aerosol vertical distribution on a deep convective cloud. *Atmosphere*, *12*(6), 675. https://doi.org/10.3390/atmos12060675

Zhang, R., Han, Z., Cheng, T., & Tao, J. (2009). Chemical properties and origin of dust aerosols in Beijing during springtime. *Particuology*, *7*(1), 61–67. https://doi.org/10.1016/j.partic.2008.11.003

Zhao, Q., He, K., Rahn, K. A., Ma, Y., Jia, Y., Yang, F., et al. (2010). Dust storms come to Central and Southwestern China, too: Implications from a Major Dust Event in Chongqing. *Atmospheric Chemistry and Physics*, *10*(6), 2615–2630. https://doi.org/10.5194/acp-10-2615-2010

Zheng, B., Tong, D., Li, M., Liu, F., Hong, C. P., Geng, G. N., et al. (2018). Trends in China's anthropogenic emissions since 2010 as the consequence of clean air actions. *Atmospheric Chemistry and Physics*, *18*(19), 14095–14111. https://doi.org/10.5194/acp-18-14095-2018

Zheng, J. Y., Zhang, Z. B., Garnier, A., Yu, H. B., Song, Q. Q., Wang, C. X., et al. (2022). The thermal infrared optical depth of mineral dust retrieved from integrated Caliop and IIR observations. *Remote Sensing of Environment*, *270*, 112841. https://doi.org/10.1016/j.rse.2021.112841